

Article

Genesis of Cambrian Dolomites in the Bachu Area, Tarim Basin, NW China: Constraints from Petrology, Geochemistry, and Fluid Inclusions

Zhipeng Chen ^{1,*} , Yanfei Yang ², Caiyuan Dong ³, Ningxi Li ³, Pengtao Wang ⁴, Shaohua Zhang ¹ , Wei Dang ¹ and Yun Liao ⁵

¹ School of Earth Sciences and Engineering, Xi'an Shiyou University, Xi'an 710065, China

² The Fifth Oil Production Plant, Changqing Oilfield Company, Xi'an 710299, China

³ Research Institute of Petroleum Exploration & Development, PetroChina, Beijing 100083, China

⁴ Sinopec Green Source Thermal Energy Development Co., Ltd., Xianyang 712000, China

⁵ State Key Laboratory of Oil and Gas Reservoir Geology and Exploitation, Chengdu University of Technology, Chengdu 610059, China

* Correspondence: zpchen@xsyu.edu.cn

Abstract: The dolomitization of carbonate rocks has always been a hot topic in the study of the dolomite reservoir. In this study, the genesis of Cambrian dolomite in the Bachu area, Tarim Basin, was assessed through petrographic examinations, isotope compositions (C, O, and Sr), trace and rare earth elements, and fluid inclusion microthermometry. Microscopic analysis revealed three types of dolomites: very fine-crystalline, nonplanar dolomite (D1); fine-crystalline, nonplanar to planar-s dolomite (D2); and medium- to coarse-crystalline, planar-e to planar-s dolomite (D3). D1 dolomite exhibits well-preserved original sedimentary features, such as algal laminae, stromatolite, and evaporite streak, and is characterized by the $^{87}\text{Sr}/^{86}\text{Sr}$ value and $\delta^{18}\text{O}$ value in equilibrium with the coeval seawater, its high Sr and Na content, and its low Mn content. This indicates that D1 dolomite is primarily a penecontemporaneous dolomite in tidal flat or lagoon environments, and its dolomitizing fluid is mainly evaporated mesosaline to penesaline seawater. D2 dolomite shows ghosts of precursor particles; features $\delta^{13}\text{C}$ values in equilibrium with the coeval seawater, high $^{87}\text{Sr}/^{86}\text{Sr}$ values, low Sr content, and positive Eu anomaly; and is widely distributed close to stylolite. This illustrates that D2 dolomite was principally formed by seepage–reflux dolomitization, and is closely related to hydrothermal activity and pressure dissolution. D3 dolomite displays a crystal texture with a cloudy core and compositional zoning, and the original sedimentary fabrics cannot be identified. It has similar $\delta^{13}\text{C}$ values and REE patterns to the calcite precipitated from coeval seawater, high $^{87}\text{Sr}/^{86}\text{Sr}$ values, low Sr contents and high Mn/Sr ratios, which suggests that D3 dolomite is chiefly related to the recrystallization of the precursor dolomite during the deep burial stage, and the deep circular brine provides Mg ions through the fluid–rock reaction. This study shows that the Cambrian dolomite in the Bachu area is mainly formed in the coeval seawater environment during the penecontemporaneous and shallow burial stages, and has extensively suffered from recrystallization and burial diagenesis due to long-term deep burial, which was further strengthened in the fracture-enriched area.

Keywords: dolomitization; recrystallization; strontium isotope; hydrothermal fluid; Tarim Basin



Citation: Chen, Z.; Yang, Y.; Dong, C.; Li, N.; Wang, P.; Zhang, S.; Dang, W.; Liao, Y. Genesis of Cambrian Dolomites in the Bachu Area, Tarim Basin, NW China: Constraints from Petrology, Geochemistry, and Fluid Inclusions. *Minerals* **2022**, *12*, 1157. <https://doi.org/10.3390/min12091157>

Academic Editors: Vincent V. Barbin and Frédéric Marin

Received: 14 August 2022

Accepted: 12 September 2022

Published: 14 September 2022

Publisher's Note: MDPI stays neutral with regard to jurisdictional claims in published maps and institutional affiliations.



Copyright: © 2022 by the authors. Licensee MDPI, Basel, Switzerland. This article is an open access article distributed under the terms and conditions of the Creative Commons Attribution (CC BY) license (<https://creativecommons.org/licenses/by/4.0/>).

1. Introduction

Dolomite is a significant target for oil and gas exploration worldwide. The thickness of Cambrian dolostone strata in the Tarim Basin is more than 1000 m, and its distribution area is nearly $15 \times 10^4 \text{ km}^2$ [1,2]. Recently, a large volume of natural gas has been discovered in the Tarim Basin, and the Cambrian dolomite is considered a crucial reservoir [1–4]. In general, the formation of dolomite is a complex process, which may be continuous

or intermittent. A dolomite geobody may have experienced multiple stages or types of dolomitization, including a variety of dolomite of different origins [5,6]. Dolomitization can destroy, maintain or enhance porosity, and its effects vary with geological and chemical kinetic reaction conditions [7–9]. Therefore, understanding the formation environment and the fluid types of dolomitization is significant for predicting the distribution of favorable dolomite reservoirs.

A large amount of Mg^{2+} is required for a limestone formation to reach full dolomitization, so large-scale dolomitization often requires a high fluid–rock ratio [6,10]. This means that determining the characteristics of dolomitizing fluid is critical for identifying the origin of dolomite. The dolomitizing fluid could be evaporatively concentrated or modified seawater [11,12], connate seawater [13,14], mixed water formed by meteoric freshwater and seawater [7,15], residual brine [10,12], and deep hydrothermal fluid [16–18]. Dolomitizing fluid with different sources or migration modes represents the diverse dolomitization modes. Many researchers have studied the origin of Cambrian dolomites in the Tarim Basin through petrography and geochemistry. A series of dolomitization models have been proposed to explain the widespread occurrence of dolomitized rocks, including Sabkha-style dolomitization [15], seepage-reflux dolomitization [19], microbial dolomitization [20,21], burial dolomitization [4,19,22], marine–meteoric mixing-zone dolomitization [15], and hydrothermal dolomitization [3,4,18].

However, these studies mainly focus on specific dolomite types that are closely related to reservoirs, such as microbial dolomite or hydrothermal dolomite, or on particular layers with substantial oil and gas breakthroughs, such as the Xiaoerbulake Formation [21]. Dolomitization is a dynamic and continuous process. Previously formed dolomites are adjusted according to changes in temperature, pressure, and fluid properties in the late stage, superimposing multiple dolomitization mechanisms [18,23,24]. In addition, distinct from the central and eastern Tarim Basin, the Cambrian evaporite series frequently appears in the Bachu area, which means that the connate seawater may widely exist in the strata and may be driven by tectonic activity and geothermal variation [25]. Meanwhile, the migration and circulation of tremendous dolomitizing fluid in a relatively closed diagenetic system involves the whole carbonate rock series and surrounding rocks.

In this study, we carried out detailed petrographic examinations, isotope compositions (O, C, and Sr), trace and rare earth elements, and fluid inclusion microthermometry of the Cambrian dolomite in the Bachu area. This aimed to identify different types of dolomites and to gain an in-depth understanding of the dolomitizing fluid and dolomitization process responsible for the formation of Cambrian dolostone. This study is also of great significance for predicting the distribution of dolomite reservoirs.

2. Geological Setting

The Tarim Basin is a polycyclic superimposed basin composed of Paleozoic cratonic sub-basins, as well as Mesozoic and Cenozoic foreland sub-basins [1,2,26,27]. It is also a remarkable oil- and gas-rich inland basin in China with an area of 56×10^4 km². According to the present tectonic configuration, the Tarim Basin can be divided into four depressions (Kuqa, north, southwest, and southeast) and three uplifts (Tabei, central, and southeast). The Bachu area, also known as the Bachu lift, located in the northwestern part of the central uplift (Figure 1A), is a fault uplift sandwiched between two high-dip thrust faults [2]. The Bachu area initiated the prototype of the uplift in the Early Hercynian and finally took shape in the Middle Himalayan Range [27].

The Cambrian strata in the Tarim Basin can be divided into Lower, Middle, and Upper units [15,23]. The Lower Cambrian comprises the Yuertusi Formation (E_{1y}), Xiaoerbulake Formation (E_{1x}), and Wusongger Formation (E_{1w}), which features siliciclastic rocks, dolomites, and limestones. The Middle Cambrian consists of the Shayilike Formation (E_{2s}) and Awatage Formation (E_{2a}), characterized by thick interbedded layers of gypsum, salt, dolomite, and limestone. The Upper Cambrian is composed of the Xiaqiulitage Formation (E_{3x}), which is dominated by thick dolomites and a small number of limestones (Figure 1B).

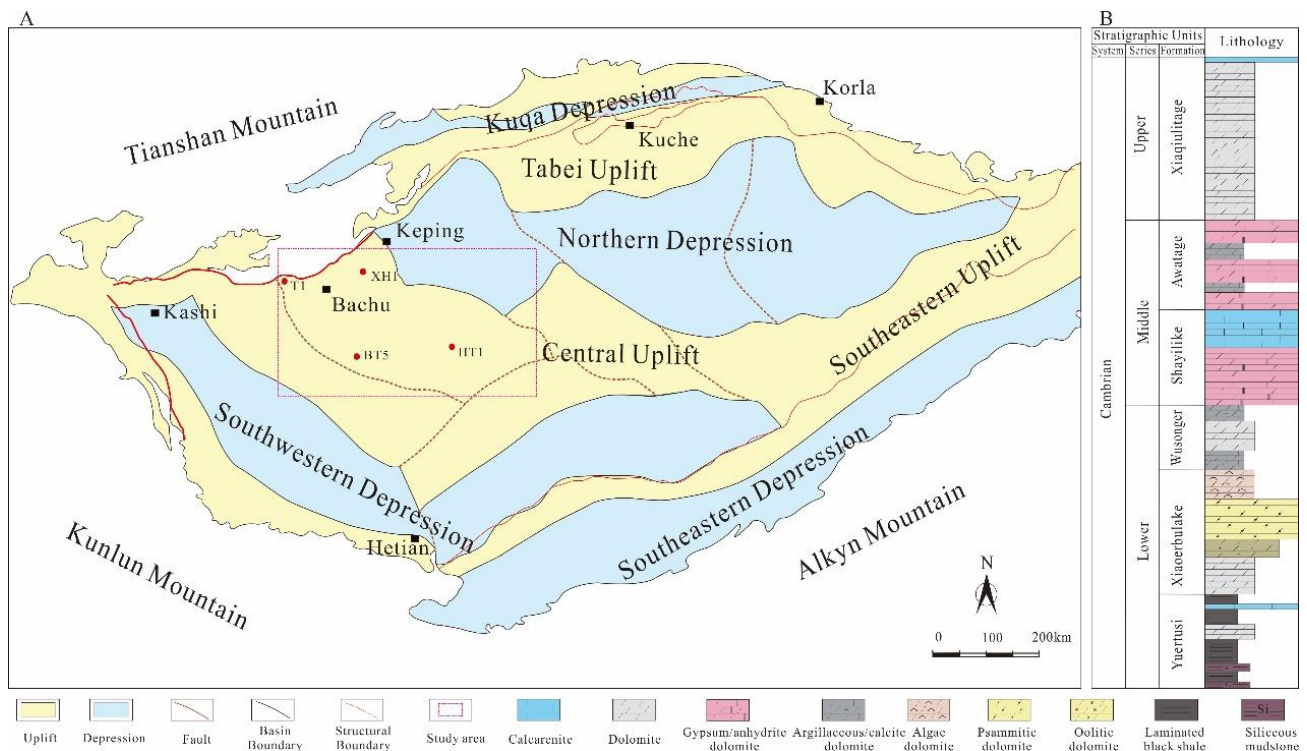


Figure 1. (A) Sketch map showing the geotectonic components of the Tarim Basin (modified from Du et al. (2017) [28]); (B) generalized diagram showing the stratigraphy and lithofacies of the Cambrian successions in the Bachu area (modified from Hu et al. (2019) [22]).

During the Cambrian period, the Tarim Basin was located in a low-latitude zone near the equator with a hot and arid climate [26,27]. The eastern Tarim Basin is mainly an under-compensated deep-water basin, while the western Tarim Basin is dominated by a shallow-water carbonate platform [23,27,29]. The Bachu area was lying on the edge of a southwest paleo uplift, and its sedimentary environment frequently changed with the fluctuation of the eustatic sea level [2,15,29]. During the Early Cambrian period, the Bachu area experienced a short-term deep-water basin environment. In the Middle to Late Cambrian, the study area gradually evolved from a restricted platform to an evaporative platform due to the strengthening of evaporation. During the Upper Cambrian, the Bachu area was dominated by open platform with the rising eustatic sea level. The Cambrian in the Bachu area is generally characterized as an evaporation platform-restricted platform-open platform depositional system [2,15]. The sedimentary environment of the study area was primarily the lime, limestone-dolomite, gypsum-dolomite, and dolomite tidal flats of the restricted platform in the Lower Cambrian, and converted to the intertidal tidal flats and saline lacustrine of the evaporative platform in the Middle Cambrian, and transformed to the shoal and dolomite tidal flats of the open platform in the Upper Cambrian [30,31].

The Tarim Basin has experienced multiple evolutionary stages induced by Caledonian, Hercynian, Indosinian, and Himalayan tectonic events. The burial and thermal history in the Bachu area shows that the Cambrian carbonate rocks suffered three significant uplifts during the continuous subsidence process (Figure 2). During the Cambrian to the Early Ordovician, the basin was in the extension period of the passive continental margin. The tectonic subsidence rate was relatively faster after the deposition [32]. The Cambrian carbonate rocks in the study area subsided rapidly after being deposited, with a burial depth of 4000–5500 m. During the Late Ordovician to the Early Carboniferous, the first uplift episode occurred concerning the Late Caledonian Orogeny, with a tectonic uplift of approximately 1000 m. During the Late Devonian, the second uplift episode occurred in association with the Early Hercynian Orogeny, with a tectonic uplift of nearly 300 m.

During the Late Cretaceous, the third uplift episode took place during the Late Yanshan Orogeny, with a tectonic uplift of approximately 800 m.

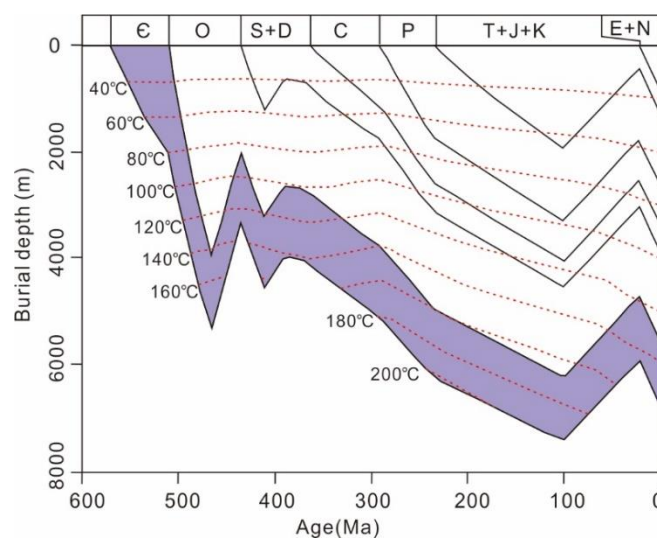


Figure 2. Burial history of the Cambrian succession in the Bachu area based on well HT1 (modified from Qiu et al. (2012) [32]).

3. Material and Methods

More than one hundred samples were collected from wells HT1, BT5, T1, and XH1 in the Bachu area, Tarim Basin. Based on the detailed description and macro-petrographic observations, we selected forty-five typical Cambrian dolomite samples to ensure a more detailed study. There were nineteen samples from ϵ_{3x} , fourteen samples from ϵ_{2a} , six samples from ϵ_{1w} , and six samples from ϵ_{1x} . The samples were polished into thin sections for detailed micro-petrographic studies under the Zeiss Axio Imager A2 microscope. The morphology, structure and composition of the minerals were examined using a scanning electron microscope (SEM).

For the ordering state of dolomite, the samples were cut into squares, and then the position of pure dolomite particles was determined via SEM analysis. The dolomite particles were extracted and ground into powders smaller than 75 μm . The dolomite powders were measured in terms of ordering reflections using the Rigaku D/Max RAPID X-ray diffractometer. The ordering state of dolomite is usually quantified by two methods: the ratio of D-(015) and D-(110) peaks [33] and the plot of D-(104) peak versus MgCO_3 mol% [34]. The former method is mainly applicable to relatively pure dolomite due to the influence of detrital mineral phases, while the latter is more suitable for weakly ordered dolomite. There are relatively few detrital minerals in the Cambrian dolomite in the Bachu area, and the ordering degree of dolomite is generally high due to the deep burial diagenesis. Therefore, the ordering state is reported as the ratio of the D-(015) and D-(110) peaks in this study [35,36]. The petrographic identification and ordering analysis of dolomite were completed in the Shaanxi Key Laboratory of Petroleum Accumulation Geology.

The measurements of trace and REE elements ($n = 43$) were conducted in the State Key Laboratory of Marine Geology, Tongji University. For the analysis of trace elements and REEs, the powdered samples were pretreated with $\text{HF} + \text{HNO}_3$ mixed acid and diluted with ultrapure H_2O . The diluted solution was tested using Thermo Fisher VG-X7 inductively coupled plasma mass spectrometry (ICP-MS). During the isotope test, 1 ppb Rh and Re elements were used as internal standards to monitor the instrument's stability, and international standards (GSR-5, GSR-6, and GSD-9) and blank samples were used for instrument calibration. The relative standard deviations (RSD %) of the major elements were less than 1%, while those of the trace elements and REEs were less than 2%. The REEs

of samples were normalized using McLennan's (1989) Post-Archean Average Shale (PAAS) data [37]. Eu and Ce anomaly values were determined using the following equation [38]:

$$\text{Eu}/\text{Eu}^* = \text{Eu}_{\text{SN}} / (0.67 \text{Sm}_{\text{SN}} + 0.33 \text{Tb}_{\text{SN}}) \quad (1)$$

$$\text{Ce}/\text{Ce}^* = \text{Ce}_{\text{SN}} / (0.5 \text{La}_{\text{SN}} + 0.5 \text{Pr}_{\text{SN}}) \quad (2)$$

where Eu_{SN} , Sm_{SN} , Tb_{SN} , Ce_{SN} , La_{SN} , and Pr_{SN} are PAAS-normalized Eu, Sm, Tb, Ce, La, and Pr, respectively.

The carbon and oxygen isotope analyses ($n = 44$) were conducted at Guangzhou Kesheng Instrument Technology Company, China. The powdered sample was pretreated, dried, mixed with concentrated phosphoric acid, and placed under a temperature of 90 °C for 1000 s. The generated CO_2 was injected into the water trap at -70 °C, and the external and internal cold fingers, at -162 °C. The $\delta^{13}\text{C}$ and $\delta^{18}\text{O}$ of the equilibrated CO_2 gas were measured using a GV IsoPrime II stable isotope ratio mass spectrometer (IRMS) and reported using the standard label of the Vienna Peedee Belemnite (VPDB) standard. The international standard samples NBS19 and IAEA-CO-1 were used for calibration. The internal accuracies of $\delta^{13}\text{C}$ and $\delta^{18}\text{O}$ were lower than 0.005 and 0.009‰, respectively. The oxygen isotope composition of the diagenetic fluid was calculated using the calcite–fluid and dolomite–fluid fractionation equations of Land (1983) [5], as follows:

$$10^3 \ln \alpha_{\text{calcite-fluid}} = 2.78 \times 10^6 \text{T}^{-2} - 2.89 \quad (3)$$

$$10^3 \ln \alpha_{\text{dolomite-fluid}} = 3.2 \times 10^6 \text{T}^{-2} - 3.30 \quad (4)$$

where T is the temperature in Kelvin. Meanwhile, the conversion from $\delta^{18}\text{O}$ (VPDB) to $\delta^{18}\text{O}$ (VSMOW) applied the equation of Kim et al. (2015) [39], as follows:

$$\delta^{18}\text{O} (\text{VPDB}) = 1.03091 \times \delta^{18}\text{O} (\text{VSMOW}) - 30.92 \quad (5)$$

The strontium isotope analysis ($n = 9$) was performed at the State Key Laboratory of Continental Dynamics, Northwestern University. The powdered samples were dissolved in 2.5 N HCl at 90 °C. The strontium in acidic solution was separated on a chromatographic column utilizing an ion exchange resin. The calibration was performed with the international standard samples NBS987, AGV-2, and BHVO-2. The analyzed samples were separated and purified in an ultra-clean laboratory, evaporated to dryness in a polytetrafluoroethylene beaker, dissolved in ultra-pure HCl, and separated and enriched using a cation exchange resin column. An iso-compass was used for data processing [40].

The microthermometry measurement of fluid inclusions ($n = 6$) was carried out in the Shaanxi Key Laboratory of Petroleum Accumulation Geology. The homogenization temperature (T_h) and final melting temperatures (T_m) of two-phase (liquid–vapor) fluid inclusions were determined in double-polished thin sections (50 μm thick) using an Axioskop 40A Pol microscope with a Linkam THM600 heating–cooling stage. Calibration was performed using synthetic H_2O and CO_2 fluid inclusion standards with accuracies of ± 1 °C at 300 °C and ± 0.1 °C at -56.6 °C, respectively. The occurrence, size, and liquid/vapor ratios of fluid inclusions were used to determine their origin. The heating experiment was carried out before the cooling experiment to reduce the risk of bursting fluid inclusions. The salinity was determined from T_m using the equation of Bodnar (1993) [41], as follows:

$$\text{wt}\% \text{NaCl} = 1.78 \times T_m - 0.0442 \times (T_m)^2 + 0.000557 \times (T_m)^3 \quad (6)$$

where T_m is the final melting temperature of fluid inclusions.

4. Results

4.1. Petrography

Based on the crystal size, distribution, and surface morphology of Cambrian dolomites in the Bachu area [42], three types of matrix dolomite textures were identified: (1) very fine-

crystalline, nonplanar dolomite (D1); (2) fine-crystalline, nonplanar to planar-s dolomite (D2); and (3) medium- to coarse-crystalline, planar-e to planar-s dolomite (D3).

4.1.1. D1 Dolomite

D1 dolomite commonly comprises dolomicrite to closely packed near-micritic crystals with a size of 20–60 μm , showing nonplanar to planar-s textures. Slightly coarse dolomite crystals typically display subhedral crystal surfaces, which are distributed along the bedding as scattered or floating dolomite crystals (Figure 3A). It is common for micritic dolomite laminae to be interbedded with salt and anhydrite laminae, which were severely deformed in this study due to sliding or flow induced by overlying pressure (Figure 3B). Cryptocrystalline pyrites, which indicate a reducing environment, were mostly disseminated in the intercrystalline pores (Figure 3C). D1 dolomite commonly preserved the well-defined sedimentary fabrics of precursor limestone and fossil remains, such as horizontal or ripple-like bedding (Figure 3A), ooid or debris (Figure 3D), lamellar stromatolites (Figure 3E) and algal grains (Figure 3F). The dolomite cation ordering ranged from 0.61 to 1.00 ($n = 4$), with an average of 0.83 (Table 1). D1 dolomite accounted for approximately 50% of the studied samples and was more common in the Xiaqiulitage, Awatage, and Wusongger Formations.

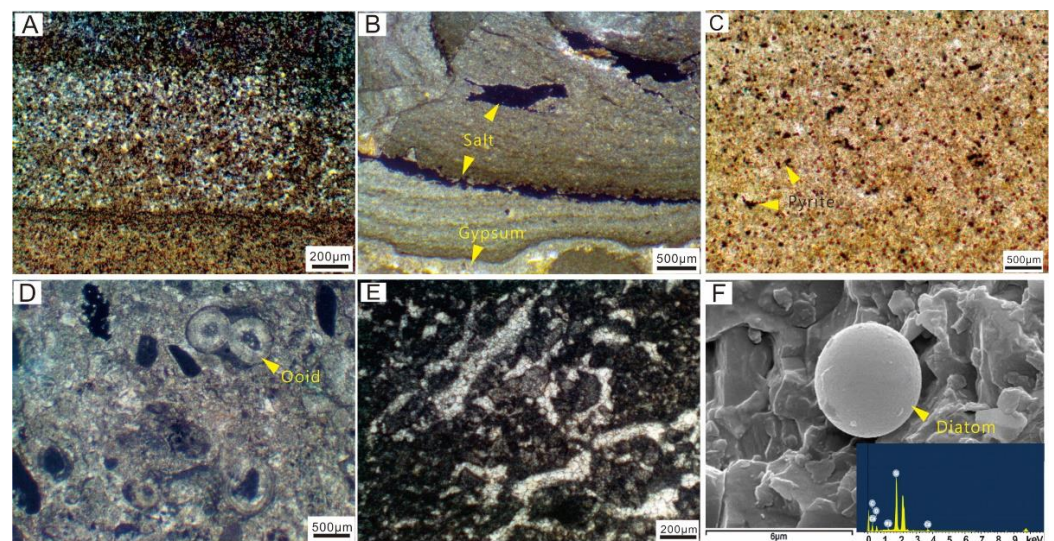


Figure 3. D1 dolomite: (A) very fine-crystalline dolomite with horizontal bedding, well BT5, 4742.29 m, E_{3x} , under plane-polarized light (PPL). (B) Micritic dolomite laminae interbedded with salt and anhydrite laminae (arrows), well HT5, 6162 m, E_{2a} , under PPL. (C) Cryptocrystalline pyrites (arrows) disseminated within intercrystalline pores, well HT1, 6433 m, E_{2a} , under PPL. (D) Precursor limestone ooid (arrows) replaced by dolomicrite, well BT5, 4742 m, E_{3x} , under PPL. (E) Microcrystalline dolomite with a stromatolitic structure, well XH1, 5436 m, E_{1w} , under PPL. (F) Diatom chondrite (arrows) in microcrystalline dolomite, well XH1, 5442 m, E_{1x} , under scanning electron microscope-second electron (SEM-SE).

Table 1. Summary statistics of major elements, trace elements, and rare earth elements of the Cambrian dolomites in the Bachu area, Tarim Basin.

Sample	Dolomite Classes	Formation	Cation ordering	Na (ppm)	Fe (ppm)	Mn (ppm)	Sr (ppm)	Mn/Sr	La (ppm)	Ce (ppm)	Pr (ppm)	Nd (ppm)	Sm (ppm)	Eu (ppm)	Gd (ppm)	Tb (ppm)	Dy (ppm)	Ho (ppm)	Er (ppm)	Tm (ppm)	Yb (ppm)	Lu (ppm)	ΣREE (ppm)	Eu/Eu*	Ce/Ce*
BT5-W2	D1	E ₃ X	-	104	980	54	85	0.64	1.71	3.69	0.42	1.50	0.28	0.06	0.24	0.04	0.22	0.04	0.13	0.02	0.12	0.02	9.61	1.00	1.01
BT5-W3	D1	E ₃ X	-	178	1400	39	108	0.36	1.40	2.82	0.28	1.16	0.22	0.05	0.22	0.04	0.19	0.04	0.10	0.02	0.13	0.03	7.79	1.08	1.04
BT5-26	D1	E ₂ a	-	863	6306	80	6711	0.01	3.96	8.14	0.89	3.42	0.62	0.15	0.65	0.09	0.57	0.11	0.35	0.05	0.36	0.05	22.25	1.23	1.00
BT5-29	D1	E ₂ a	-	314	2611	34	11,056	0.00	1.34	3.34	0.32	1.31	0.24	0.09	0.26	0.04	0.21	0.05	0.12	0.02	0.11	0.01	8.66	1.81	1.18
BT5-31	D1	E ₂ a	0.61	698	8994	101	1114	0.09	4.83	9.58	1.04	3.95	0.76	0.14	0.72	0.11	0.61	0.13	0.40	0.06	0.39	0.06	25.93	0.94	0.99
BT5-32	D1	E ₂ a	-	366	6381	64	1377	0.05	3.51	6.32	0.68	2.53	0.47	0.08	0.43	0.06	0.34	0.08	0.22	0.03	0.25	0.04	16.83	0.90	0.94
BT5-39	D1	E ₂ a	-	32,785	6379	109	756	0.14	4.50	9.60	1.17	4.56	0.88	0.20	0.95	0.14	0.82	0.17	0.48	0.07	0.45	0.06	28.24	1.12	0.96
BT5-45	D1	E ₂ a	-	1660	13,028	151	356	0.42	16.16	34.90	3.87	15.05	2.94	0.55	2.72	0.39	2.32	0.45	1.30	0.18	1.23	0.18	93.02	0.98	1.02
BT5-48	D1	E ₁ W	0.94	480	4055	133	431	0.31	5.61	12.36	1.24	4.85	0.95	0.23	1.03	0.14	0.75	0.14	0.38	0.05	0.29	0.04	31.71	1.22	1.08
BT5-50	D1	E ₁ W	-	907	7570	146	474	0.31	10.63	23.14	2.56	10.37	2.23	0.49	2.18	0.32	1.83	0.36	1.02	0.13	0.79	0.12	64.08	1.12	1.02
BT5-08	D1	E ₃ X	-	486	2520	31	111	0.28	1.09	2.22	0.23	0.90	0.19	0.04	0.16	0.03	0.13	0.03	0.08	0.01	0.07	0.01	5.94	1.04	1.02
BT5-W4	D1	E ₃ X	-	82	980	62	92	0.67	1.17	2.44	0.26	0.88	0.25	0.07	0.21	0.03	0.20	0.03	0.10	0.01	0.09	0.02	6.63	1.46	1.03
BT5-36	D1	E ₂ a	1.00	220	3171	48	1440	0.03	1.29	2.43	0.28	1.02	0.18	0.03	0.20	0.02	0.15	0.02	0.07	0.01	0.05	0.01	6.50	0.92	0.93
HT1-08	D1	E ₂ a	0.77	261	387	23	94	0.25	1.00	2.16	0.20	0.82	0.15	0.04	0.16	0.02	0.12	0.02	0.07	0.01	0.06	0.01	5.53	1.39	1.12
HT1-09	D1	E ₂ a	-	416	2998	45	616	0.07	2.51	4.45	0.46	1.62	0.23	0.06	0.24	0.03	0.14	0.03	0.08	0.01	0.06	0.01	10.69	1.37	0.95
HT1-10	D1	E ₂ a	-	664	1659	37	328	0.11	1.40	2.61	0.28	1.09	0.16	0.04	0.20	0.02	0.11	0.02	0.05	0.01	0.04	0.01	6.69	1.33	0.96
BT5-54	D2	E ₁ W	-	341	1301	213	123	1.73	0.68	0.97	0.10	0.39	0.08	0.02	0.09	0.01	0.07	0.01	0.04	0.01	0.03	0.01	2.97	1.33	0.84
BT5-55	D2	E ₁ W	1.00	345	2674	216	121	1.79	1.02	1.49	0.16	0.69	0.10	0.02	0.12	0.02	0.10	0.03	0.07	0.01	0.07	0.01	4.71	0.90	0.84
BT5-56	D2	E ₁ W	-	260	1512	210	111	1.89	0.87	1.46	0.18	0.69	0.15	0.03	0.15	0.02	0.12	0.02	0.06	0.01	0.05	0.01	4.59	1.04	0.85
BT5-57	D2	E ₁ W	0.93	225	1438	177	565	0.31	0.77	1.35	0.17	0.75	0.20	0.04	0.20	0.03	0.14	0.02	0.07	0.01	0.04	0.01	4.66	1.01	0.86
XH1-2	D2	E ₁ X	0.93	240	2039	178	222	0.80	1.49	3.82	0.41	1.71	0.35	0.08	0.40	0.06	0.37	0.08	0.20	0.03	0.17	0.02	11.12	1.09	1.12
XH1-5	D2	E ₁ X	-	404	3448	132	49	2.67	2.51	5.61	0.63	2.59	0.54	0.11	0.56	0.08	0.44	0.09	0.24	0.03	0.19	0.03	16.24	1.02	1.03
XH1-6	D2	E ₁ X	0.82	310	1128	85	594	0.14	1.35	3.02	0.36	1.48	0.33	0.06	0.32	0.04	0.27	0.05	0.15	0.02	0.11	0.02	9.26	0.98	1.00
XH1-8	D2	E ₁ X	-	459	5296	268	256	1.05	8.19	11.25	1.64	6.44	1.16	0.22	1.17	0.16	0.98	0.21	0.62	0.09	0.55	0.08	41.42	0.98	0.71
BT5-05	D2	E ₃ X	-	205	2083	46	77	0.59	0.80	1.56	0.17	0.75	0.17	0.25	0.16	0.02	0.13	0.02	0.06	0.01	0.05	0.01	4.75	7.97	0.98
BT5-W1	D2	E ₃ X	-	100	420	54	77	0.70	0.74	1.07	0.12	0.45	0.11	1.00	0.14	0.02	0.06	0.02	0.03	0.01	0.05	0.04	4.36	42.35	0.83
BT5-06	D2	E ₃ X	-	162	1205	33	65	0.51	0.54	1.06	0.11	0.45	0.10	0.03	0.10	0.01	0.07	0.01	0.04	0.01	0.02	0.01	2.90	1.70	1.00
BT5-W5	D2	E ₃ X	-	260	1540	54	46	1.19	1.03	1.99	0.22	0.79	0.12	0.35	0.30	0.03	0.14	0.03	0.10	0.02	0.09	0.02	6.11	12.07	0.97
BT5-09	D2	E ₃ X	0.98	333	1541	45	53	0.85	0.81	1.57	0.16	0.60	0.10	0.03	0.10	0.02	0.10	0.02	0.06	0.01	0.04	0.01	4.18	1.35	1.00
BT5-10	D2	E ₃ X	-	264	1601	41	85	0.48	0.99	1.82	0.18	0.74	0.13	0.03	0.13	0.02	0.12	0.03	0.07	0.01	0.05	0.01	5.09	1.15	0.99
BT5-21	D3	E ₃ X	0.89	396	2839	32	132	0.24	2.91	6.11	0.67	2.57	0.52	0.08	0.47	0.06	0.38	0.07	0.21	0.03	0.17	0.03	16.08	0.84	1.01
BT5-22	D3	E ₃ X	-	264	1368	34	62	0.55	0.57	1.10	0.12	0.49	0.08	0.02	0.08	0.01	0.07	0.01	0.04	0.01	0.03	0.01	3.05	1.33	0.97
BT5-24	D3	E ₃ X	0.99	329	1589	31	81	0.38	0.86	1.72	0.18	0.78	0.14	0.04	0.15	0.02	0.12	0.02	0.06	0.01	0.06	0.01	4.77	1.46	1.01
HT1-06	D3	E ₃ X	-	769	2363	24	61	0.38	1.08	2.35	0.25	0.94	0.17	0.04	0.20	0.03	0.15	0.03	0.09	0.01	0.08	0.01	6.23	1.11	1.04
BT5-14	D3	E ₃ X	1.00	693	3855	33	106	0.31	3.52	6.47	0.89	3.42	0.70	0.16	0.70	0.10	0.57	0.11	0.33	0.05	0.33	0.05	20.20	1.16	0.84
BT5-17	D3	E ₃ X	0.89	403	3682	48	64	0.75	1.64	3.33	0.38	1.54	0.33	0.06	0.32	0.05	0.28	0.06	0.16	0.02	0.14	0.02	9.69	0.91	0.98
BT5-19	D3	E ₃ X	0.83	446	2624	38	102	0.38	2.26	4.73	0.56	2.11	0.41	0.09	0.41	0.06	0.34	0.06	0.19	0.03	0.17	0.02	13.04	1.11	0.97
T1-4	D3	E ₃ X	0.95	340	655	49	145	0.34	1.23	2.32	0.23	0.93	0.16	0.03	0.17	0.02	0.14	0.03	0.08	0.01	0.06	0.01	6.18	1.00	1.00
T1-5	D3	E ₃ X	0.84	321	2382	43	157	0.28	2.06	4.54	0.48	1.87	0.36	0.07	0.34	0.05	0.28	0.06	0.16	0.03	0.15	0.02	11.88	1.00	1.05
BT5-27	D3	E ₂ a	0.90	132	2871	78	-	-	1.55	2.95	0.30	1.19	0.22	0.09	0.23	0.03	0.14	0.03	0.07	0.01	0.04	0.01	7.73	2.12	1.00
XH1-3	D3	E ₁ X	0.91	329	6228	165	55	3.00	4.47	9.68	1.03	4.00	0.79	0.17	0.88	0.12	0.67	0.14	0.39	0.06	0.34	0.05	26.22	1.07	1.04
XH1-4	D3	E ₁ X	-	309	5951	244	251	0.97	4.57	11.89	1.43	5.71	1.15	0.26	1.22	0.17	1.00	0.20	0.53	0.07	0.40	0.06	33.76	1.14	1.06
HT1-11	D3	E ₂ a	-	1718	2036	53	892	0.06	1.59	2.76	0.31	1.06	0.22	0.05	0.20	0.03	0.15	0.03	0.07	0.01	0.05	0.01	7.33	1.18	0.90

Note: ΣREE—total content of rare earth elements; the calculation of Eu/Eu* and Ce/Ce* follows Equations (1) and (2) [38]. “-” represents no data.

4.1.2. D2 Dolomite

D2 dolomite crystals are generally euhedral to subhedral, with a size of 60–250 μm , plane-to-straight crystal surfaces, and well-defined crystal boundaries. In hand specimens, D2 dolomite usually shows sedimentary features with dark and light gray grains or laminae, but the original sedimentary fabric of the limestone precursor is difficult to identify (Figure 4A). Differences in the shades of grains or laminae often represent distinctions in the crystallization of dolomite. This type of dolomite shows residual grain structure under the microscope, and the grain profile is clearer than that of the hand specimens (Figure 4B–D). Grains with cloudy cores and clear rims (Figure 4C) and grains with ghost outlines of precursor limestone (Figure 4D) are common in D2 dolomite, and some grains are elliptical due to mild compaction. The grains are composed of tightly packed euhedral–subhedral dolomite crystals, which are similar in size and have curved, jagged, or other irregular intercrystalline boundaries. In addition, D2 dolomites are also widely distributed along stylolites or dissolution fractures (Figure 4E,F). The fractures and vugs are partially filled with acicular anhydrite, authigenic quartz, dolomite, and calcite cements. The dolomite cation ordering varies from 0.82 to 1.00 ($n = 5$), with an average of 0.93. D2 dolomite comprises approximately 30% of all dolomites and is particularly widespread in the Xiaqiulitage and Xiaerbulake Formation.

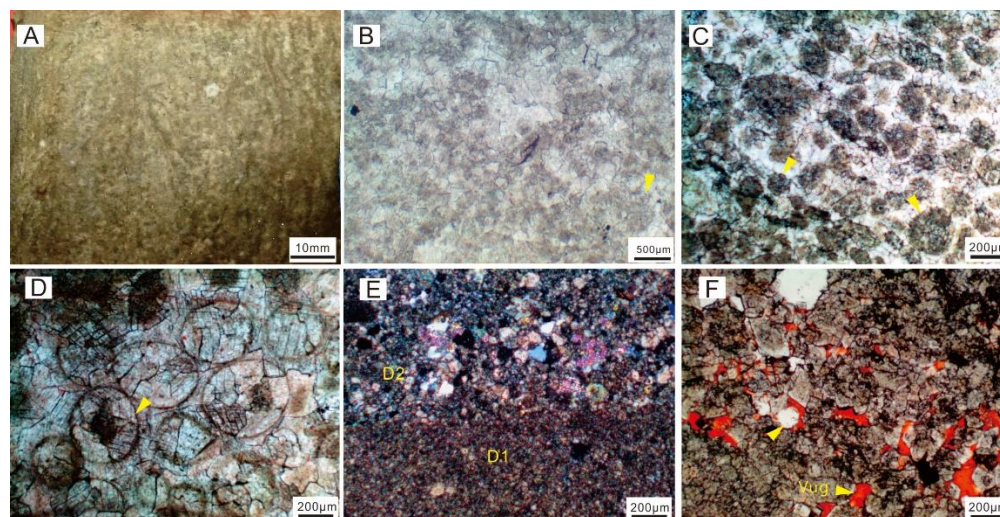


Figure 4. D2 dolomite: (A) Core photograph of fine-crystalline arenite dolomite, well HT1, 6437.30 m, E_2a . (B) Tightly packed dolomite crystals with curved surfaces show fuzzy allochem ghost (arrows), well BT5, 4802.66 m, E_3x , under PPL. (C) Ooid grains with cloudy cores and clear rims (arrows), well HT1, 6161.40 m, E_2a , under PPL. (D) Precursor deposit structure (granule ghost, arrows), well HT1, 6162.60 m, E_1x , under PPL. (E) Very fine-crystalline dolomite and fine-crystalline dolomite are distributed on different sides of the stylolite, well BT5, 5644.24 m, E_1w , under PPL. (F) Fine-crystalline dolomite crystals distributed around dissolution fractures, which are partially filled with calcite and pyrite (arrows), well BT5, 5787.63 m, E_1w , under PPL.

4.1.3. D3 Dolomite

D3 dolomite crystals are commonly 250 μm to 1 mm in size and have planar-s to planar-e structures. They primarily comprise rhombohedral or saddle-shaped crystals with the textures of cloudy cores (Figure 5A) or compositional zoning (Figure 5B,C). In addition, the original sedimentary fabric of the precursor limestone is generally difficult to identify. D3 dolomite with curved crystal planes and a tightly packed texture is typically found near fault/fracture zones (Figure 5D,E). Most intercrystalline pores and dissolution pores could be recognized under the optical microscope or scanning electron microscope, locally or entirely occluded by calcite, dolomite, and gypsum (Figure 5A–F). The dolomite cation ordering shows a range from 0.83 to 1.00 ($n = 9$), with an average of 0.91. D3 dolomite

mainly occurs in the Xiaqiulitage Formation, accounting for approximately 20% of the total dolomite in the study area.

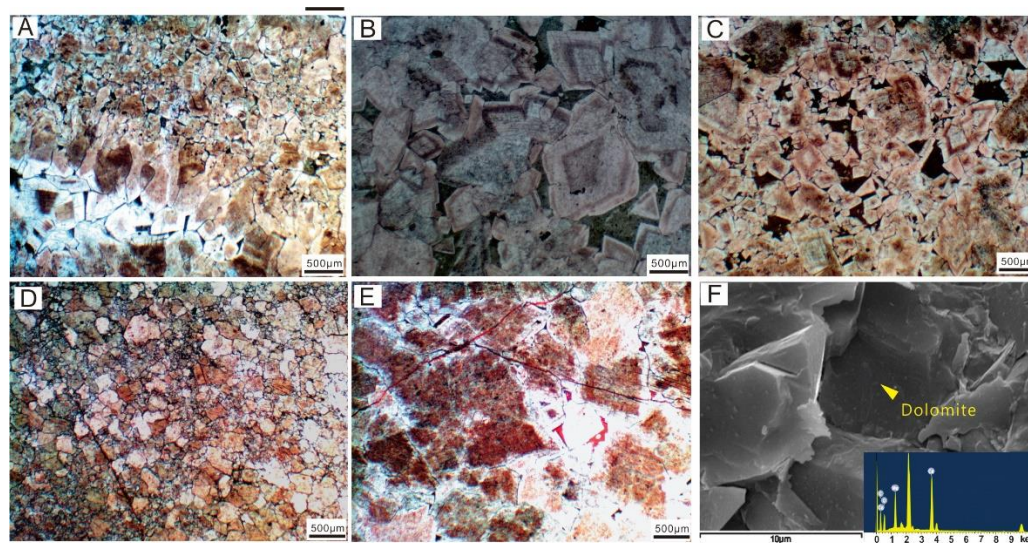


Figure 5. D3 dolomite: (A) rhombohedral-shaped crystals with cloudy cores and well-defined edges, well BT5, 4742.29 m, ϵ_3x , under PPL. (B) Coarse dolomite crystals with compositional zoning, well T1, 3181 m, ϵ_3x , under PPL. (C) Floating dolomite crystals, well BT5, 4810.65 m, ϵ_3x , under PPL. (D) D3 dolomite with curved crystal planes and a tightly packed texture, well XH1, 5436.00 m, ϵ_1x , under PPL. (E) Intercrystalline pores occluded by calcite, well T1, 3678.15 m, ϵ_3x , under PPL. (F) Pores among the coarse dolomite crystal, well XH1, 5442 m, ϵ_1x , under SEM-SE.

4.2. Element Geochemistry

Table 1 lists the summary statistics of the trace elements, REEs, and cation ordering of D1, D2, and D3 dolomites in the Bachu area, Tarim Basin.

4.2.1. Trace Element Composition

Trace elements (Sr, Na, Fe, and Mn) in dolomite are often used to indicate the properties of dolomitizing fluid. D1 dolomite possesses a high Sr abundance, ranging from 85 to 11,056 ppm (average 1572 ppm); a high Na abundance, ranging from 82 to 32,785 ppm (average 2530 ppm); a high Fe abundance, ranging from 387 to 13,028 ppm (average 4339 ppm); and a low Mn abundance, ranging from 23 to 151 ppm (average 72 ppm). D2 dolomite displays a low Sr abundance of 46 to 594 ppm (average 175 ppm), a low Na abundance of 100 to 459 ppm (average 279 ppm), a low Fe abundance of 420 to 5296 ppm (average 1945 ppm), and a high Mn abundance from 33 to 268 ppm (average 125 ppm). D3 dolomite has an intermediate Sr abundance of 55 to 12704 ppm (average 1139 ppm), a Na abundance of 132 to 1718 ppm (average 496 ppm), an Fe abundance of 655 to 6228 ppm (average 2957 ppm), and a Mn abundance of 24 to 244 ppm (average 67 ppm) (Figure 6B,C).

The Sr abundance and Mn/Sr ratio are commonly used to reflect the diagenetic alteration of Paleozoic marine carbonate rocks and the preservation of seawater information [43]. The high Sr abundance (>200 ppm) and low Mn/Sr ratio (<2.0) of carbonate rock indicate that it has not suffered diagenetic alteration, and its composition can reflect seawater information [43]. The Sr contents and Mn/Sr ratios of most D1 samples (13/18) in the study area met the criteria, indicating that their composition can basically reflect the seawater information. However, only a small number of D2 samples (4/14) and D3 samples (3/13) met the criteria, indicating that D2 and D3 dolomites may have experienced diagenetic alteration.

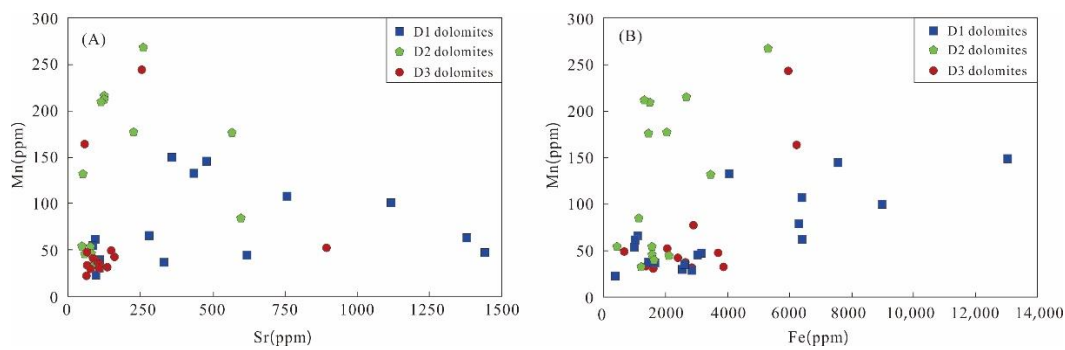


Figure 6. (A) Cross-plot of Mn versus Sr abundances in the Cambrian dolomites. (B) Cross-plot of Mn versus Fe abundance in the Cambrian dolomites.

4.2.2. Rare Earth Element (REE)

The overall REE abundance (Σ REE) of the analyzed samples yielded a broad range, from 2.90 to 93.02 ppm, with an average of 14.85 ppm, which is much smaller than the average Σ REE value of 146.37 ppm in the Upper Crust [44]. As shown in Figure 7, the PAAS-normalized REE distribution patterns of most D1, D2, and D3 dolomites were consistent with those of the limestones precipitated from the Late Ordovician seawater, which shows flat REE distribution patterns. The D1 dolomite ($n = 18$) possessed Eu/Eu* values ranging from 0.90 to 1.81 and Ce/Ce* values ranging from 0.93 to 1.18 and showed six samples of a slightly positive Eu anomaly. The D2 dolomite ($n = 14$) displayed Eu/Eu* values varying from 0.90 to 42.35 and Ce/Ce* values varying from 0.70 to 1.12 and showed six samples of a significantly positive Eu anomaly and six samples of a slightly negative Ce anomaly. The D3 dolomite ($n = 13$) had Eu/Eu* values of 0.84 to 2.11 and Ce/Ce* values of 0.84 to 1.06 and showed eight samples of a slightly positive Eu anomaly.

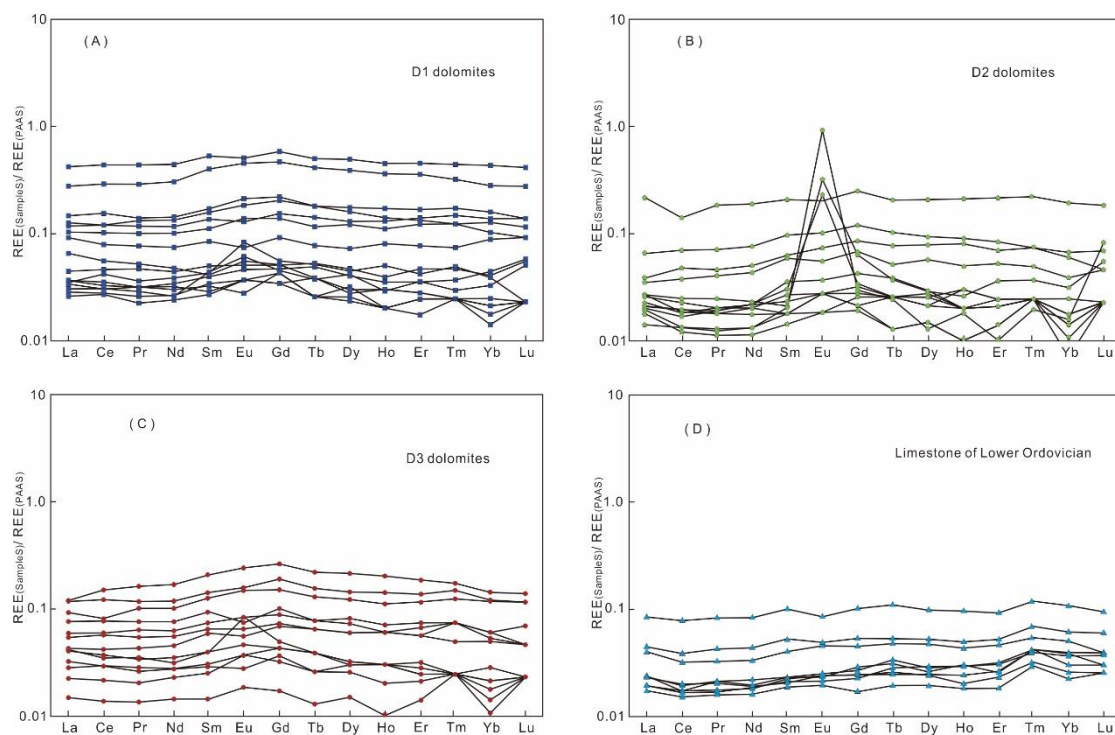


Figure 7. PAAS-normalized REE patterns of D1 dolomite (A), D2 dolomite (B), D3 dolomite (C), and limestone of Lower Ordovician (D) in the Bachu area, Tarim Basin. The PAAS data were obtained from McLennan (1989) [37]. The REE compositions of limestone of Lower Ordovician in Tarim Basin were obtained from Du et al. (2017) [28].

4.3. Isotope Geochemistry

4.3.1. Oxygen and Carbon Isotopes

The oxygen and carbon isotopic compositions of the D1, D2, and D3 dolomites from Cambrian in the Bachu area are presented in Table 2 and plotted in Figure 8. The D1 dolomite had $\delta^{18}\text{O}$ values ranging from -7.22 to -4.70 ‰ (average -6.01 ‰) and $\delta^{13}\text{C}$ values ranging from -5.00 ‰ to 0.22 ‰ (average -1.53 ‰). The D2 dolomite yielded a range of $\delta^{18}\text{O}$ values from -6.62 to -3.74 ‰ (average -5.68 ‰) and a range of $\delta^{13}\text{C}$ values from -1.10 to 0.48 ‰ (average -0.16 ‰). The D3 dolomite had $\delta^{18}\text{O}$ values of -8.13 to -5.58 ‰ (average -6.49 ‰) and $\delta^{13}\text{C}$ values of -1.97 to 0.05 ‰ (average -0.92 ‰). In addition, we collected the carbon and oxygen isotopes of Cambrian limestones in the central uplift of the Tarim Basin from Ngia et al. (2019) [31], whose $\delta^{18}\text{O}$ values ranged from -9.90 ‰ to -7.30 ‰ and $\delta^{13}\text{C}$ values ranged from -1.30 ‰ to 0.30 ‰. The reported $\delta^{18}\text{O}$ and $\delta^{13}\text{C}$ values of calcite in equilibrium with the Cambrian seawater were -6.5 to -10.0 ‰ VPDB and 1.0 to -2.0 ‰ VPDB, respectively [45,46]. The oxygen isotope fractionation from calcite to dolomite is common in the dolomitization, and its fractionation value ($\delta^{18}\text{O}_{\text{dolomite}} - \delta^{18}\text{O}_{\text{calcite}}$) is generally used as $+3$ ‰ VPDB [18,47]. It can be deduced that the $\delta^{18}\text{O}$ in Cambrian carbonate rocks ranges from -10.0 ‰ to -3.5 ‰ VPDB (Figure 8). The $\delta^{18}\text{O}$ values of Cambrian dolomite in the study area are similar to the $\delta^{18}\text{O}$ values of the estimated Cambrian marine carbonate rocks, and slightly lower than the $\delta^{18}\text{O}$ values of the estimated coeval evaporative dolomite. The ranges of $\delta^{13}\text{C}$ values in D1, D2, and D3 dolomites; ambient limestones; and coeval marine calcite are largely overlapping.

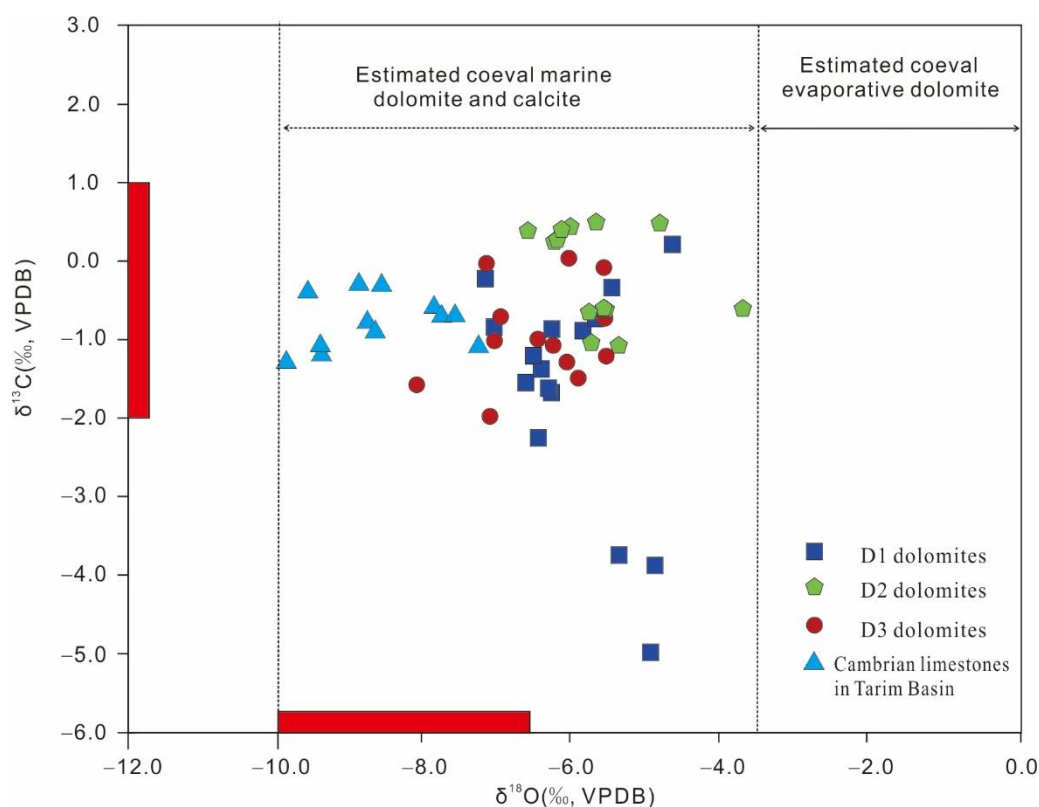


Figure 8. Cross-plot of $\delta^{18}\text{O}$ versus $\delta^{13}\text{C}$ values for D1, D2, and D3 dolomites in the Cambrian successions, Bachu area, Tarim Basin. The $\delta^{18}\text{O}$ and $\delta^{13}\text{C}$ values of Cambrian calcite are derived from Ngia et al. (2019) [31]. The isotope ranges of Cambrian marine calcite (red bars) and the $\delta^{18}\text{O}$ range of coeval evaporative dolomites (solid double arrow) are present for comparison [45,46,48]. The estimated coeval marine dolomite and calcite are calculated using the $\delta^{18}\text{O}_{\text{dolomite}} - \delta^{18}\text{O}_{\text{calcite}}$ of $+3$ ‰ VPDB (dashed double arrow) [18,47].

Table 2. Isotopic data ($\delta^{13}\text{C}$, $\delta^{18}\text{O}$, and $^{87}\text{Sr}/^{86}\text{Sr}$) of D1, D2, and D3 dolomites in the Bachu area, Tarim Basin.

Sample	Dolomite Class	Formation	Depth (m)	$\delta^{18}\text{O}$ (‰, VPDB)	$\delta^{13}\text{C}$ (‰, VPDB)	$^{87}\text{Sr}/^{86}\text{Sr}$	($\pm 2\sigma$)
BT5-W2	D1	E _{3x}	4741.75	−5.80	−0.70	-	-
BT5-W3	D1	E _{3x}	4741.83	−5.70	−0.70	-	-
BT5-26	D1	E _{2a}	5218.84	−6.50	−2.24	-	-
BT5-28	D1	E _{2a}	5219.37	−6.31	−0.88	-	-
BT5-29	D1	E _{2a}	5219.8	−6.31	−1.67	-	-
BT5-31	D1	E _{2a}	5220.55	−6.47	−1.38	0.709151	10
BT5-32	D1	E _{2a}	5221.55	−7.09	−0.86	-	-
BT5-39	D1	E _{2a}	5486.81	−5.51	−0.35	-	-
BT5-45	D1	E _{2a}	5640.03	−5.4	−3.76	-	-
BT5-48	D1	E _{1w}	5644.12	−4.94	−3.9	0.709072	9
BT5-50	D1	E _{1w}	5646.11	−4.98	−5	-	-
BT5-08	D1	E _{3x}	4742.19	−5.71	−0.74	-	-
BT5-W4	D1	E _{3x}	4742.33	−5.9	−0.9	-	-
BT5-36	D1	E _{2a}	5223.48	−7.22	−0.23	0.709039	9
BT5-42	D1	E _{2a}	5515.36	−4.7	0.2	-	-
HT1-08	D1	E _{2a}	6162.4	−6.36	−1.64	-	-
HT1-09	D1	E _{2a}	6432.5	−6.57	−1.23	-	-
HT1-10	D1	E _{2a}	6432.7	−6.66	−1.56	-	-
BT5-54	D2	E _{1w}	5782.92	−6.17	0.39	-	-
BT5-55	D2	E _{1w}	5784.32	−5.71	0.48	0.711291	11
BT5-56	D2	E _{1w}	5784.73	−6.06	0.42	-	-
BT5-57	D2	E _{1w}	5787.61	−6.62	0.36	0.711125	17
XH1-5	D2	E _{1x}	5559	−6.24	0.25	-	-
XH1-6	D2	E _{1x}	5558	−4.87	0.47	-	-
XH1-8	D2	E _{1x}	5607	−6.28	0.22	0.709162	12
BT5-05	D2	E _{3x}	4739.11	−5.81	−0.67	-	-
BT5-W1	D2	E _{3x}	4739.13	−5.60	−0.60	-	-
BT5-06	D2	E _{3x}	4739.25	−5.56	−0.62	-	-
BT5-W5	D2	E _{3x}	4802.6	−5.40	−1.10	-	-
BT5-09	D2	E _{3x}	4802.73	−3.74	−0.63	-	-
BT5-10	D2	E _{3x}	4806.81	−5.76	−1.06	-	-
BT5-21	D3	E _{3x}	4810.54	−5.58	−1.18	0.709875	10
BT5-22	D3	E _{3x}	4811.94	−5.62	−0.07	-	-
BT5-24	D3	E _{3x}	4812.49	−5.58	−0.71	0.709406	10
HT1-06	D3	E _{3x}	5760	−7.15	−1.97	-	-
BT5-14	D3	E _{3x}	4807.68	−6.29	−1.07	-	-
BT5-17	D3	E _{3x}	4808.62	−6.50	−0.99	-	-
BT5-19	D3	E _{3x}	4809.77	−6.11	−1.25	-	-
T1-4	D3	E _{3x}	3175	−8.13	−1.55	-	-
T1-5	D3	E _{3x}	3180.62	−5.97	−1.49	-	-
BT5-27	D3	E _{2a}	5219.13	−7.09	−0.98	-	-
XH1-3	D3	E _{1x}	5438.5	−7.00	−0.71	-	-
XH1-4	D3	E _{1x}	5442.16	−6.10	0.05	0.716772	15
HT1-11	D3	E _{2a}	6438.2	−7.19	0.00	-	-
F1S-5 *	LST	E _{3x}	2574.3	−8.70	−0.90	0.709354	12
F1S-9 *	LST	E _{3x}	2583.6	−8.60	−0.30	-	-
F1S-11 *	LST	E _{3x}	2792.8	−7.90	−0.60	0.709275	10
F1S-13 *	LST	E _{3x}	3748.3	−9.40	−1.10	0.709323	10
F1S16 *	LST	E _{1w}	4381.3	−9.60	−0.40	0.709098	10
T1S8 *	LST	E _{2s}	4346.3	−7.30	−1.10	-	-
T1S11 *	LST	E _{1w}	4356.4	−9.90	−1.30	0.709257	9
H4S10 *	LST	E _{2a}	5246.4	−7.60	−0.70	0.709147	9

Table 2. Cont.

Sample	Dolomite Class	Formation	Depth (m)	$\delta^{18}\text{O}$ (‰, VPDB)	$\delta^{13}\text{C}$ (‰, VPDB)	$^{87}\text{Sr}/^{86}\text{Sr}$	($\pm 2\sigma$)
H4S13 *	LST	E_2a	5443.4	−9.40	−1.20	-	-
H4S15 *	LST	E_2s	5362.5	−7.80	−0.70	-	-
H4S18 *	LST	E_1x	5733.4	−9.90	−1.30	-	-
HT1S5 *	LST	E_3x	3697.6	−8.80	−0.80	0.709285	10
HT1S6 *	LST	E_3x	3702.1	−8.90	−0.30	0.708872	11

Note: The isotopic value (*) of Cambrian limestones in Tarim Basin refers to Ngia et al. (2019) [31]. “-” represents no data.

4.3.2. Strontium Isotope

There were significant differences in the $^{87}\text{Sr}/^{86}\text{Sr}$ ratios among the three types of dolomites in the study area (Table 2, Figure 9). The D1 dolomite had $^{87}\text{Sr}/^{86}\text{Sr}$ ratios ranging from 0.709039 to 0.709151 with an average of 0.709087. The $^{87}\text{Sr}/^{86}\text{Sr}$ ratios of the D2 dolomite varied from 0.709162 to 0.711291, with an average of 0.710526. The D3 dolomite yielded $^{87}\text{Sr}/^{86}\text{Sr}$ ratios of 0.709406 to 0.716772 with an average of 0.712018. The $^{87}\text{Sr}/^{86}\text{Sr}$ ratios of D1 dolomite were all within the estimated range of $^{87}\text{Sr}/^{86}\text{Sr}$ ratios for Cambrian seawater (0.7085–0.7095) [45,46], while most D2 and D3 dolomites were not within this range.

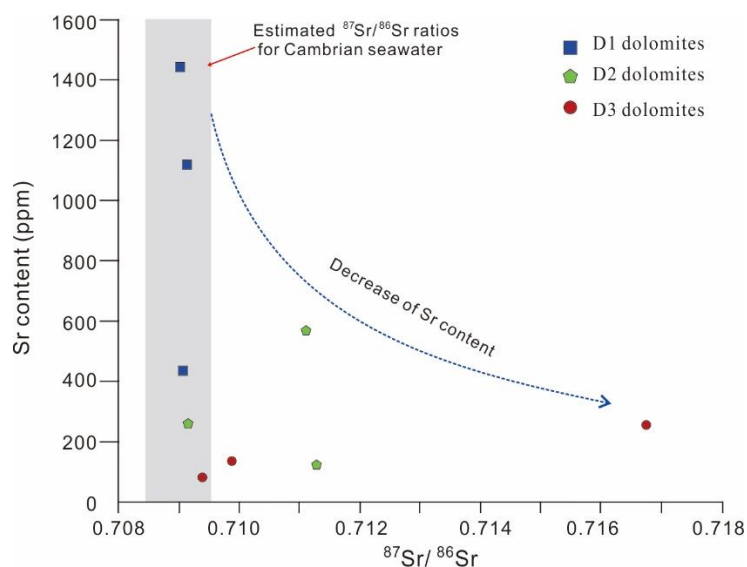


Figure 9. Cross-plot of $^{87}\text{Sr}/^{86}\text{Sr}$ versus Sr abundance for D1, D2, and D3 dolomites in the Cambrian successions, Bachu area, Tarim Basin. The strontium isotope range of coeval seawater marked in gray refers to Veizer et al. (1999) [45,46].

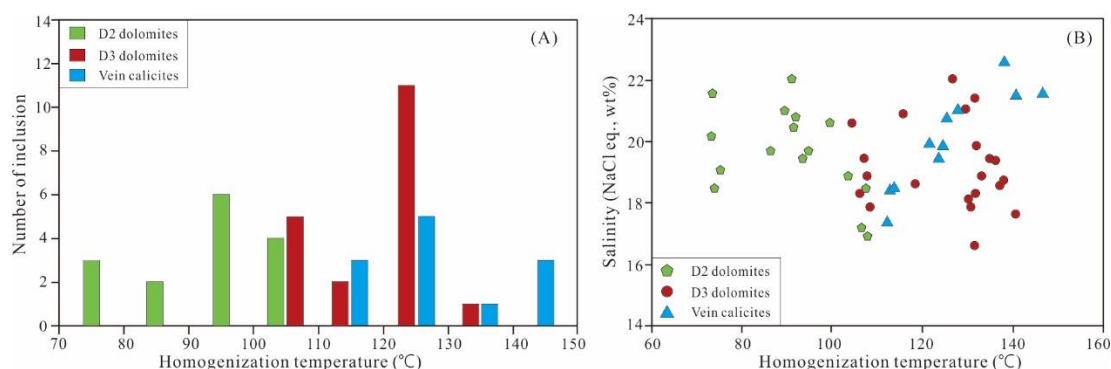
4.4. Microthermometry of Fluid Inclusions

The homogenization temperature (T_h) and final melting temperature (T_m) of two-phase (liquid–vapor) inclusions in D2 and D3 dolomite crystals were examined. The fluid inclusions were elongated or irregular in shape, ranging in size from 3 to 10 μm , with a gas–liquid ratio of 2 to 9%.

The T_h values of the D2 dolomite crystals spanned from 73.3 to 108.1 $^\circ\text{C}$ (average 91.4 $^\circ\text{C}$) and the T_m values varied from -19.2 to -13.0 $^\circ\text{C}$ (average -16.3 $^\circ\text{C}$) (Table 3; Figure 10). The salinity reckoned from the T_m values ranged from 16.9 to 21.8 wt% NaCl equivalents (average 19.6%). The D3 dolomite crystals possessed T_h values varying from 104.6 to 140.8 $^\circ\text{C}$ (average 125.4 $^\circ\text{C}$) and T_m values of -19.5 to -12.7 $^\circ\text{C}$ (average -15.7 $^\circ\text{C}$) (Table 3; Figure 10). Estimated salinity levels varied from 16.6 to 22.0 wt% NaCl equivalent (average 19.6%).

Table 3. Fluid inclusion data for D2 and D3 dolomites, and vein calcite from the Cambrian successions in the Bachu area, Tarim Basin.

Sample	Mineral Type	Number of Inclusion	Th (°C)			Tm (°C)			Salinity (NaCl eq., wt%)		
			Min.	Max.	Mean.	Min.	Max.	Mean.	Min.	Max.	Mean.
BT5-10	D2 dol	8	86.6	99.5	92.4	−9.2	−6.0	−7.3	19.4	22.0	20.5
BT5-55	D2 dol	4	73.3	75.5	74.1	−8.8	−4.8	−6.5	18.5	21.5	19.8
BT5-57	D2 dol	4	103.7	108.1	106.5	−9.8	−8	−8.6	21	22.2	21.4
BT5-21	D3 dol	8	126.8	140.8	133.9	−9.5	−3.8	−6.6	17.6	22	19.8
XH1-04	D3 dol	7	104.6	118.5	109.8	−9.3	−5	−7.3	18.6	21.9	20.4
HT1-06	D3 dol	6	130.3	136.2	132.3	−5.9	−2.7	−4.5	16.6	19.4	18.2
BT5-10	Vein-cal	5	121.7	128.1	124.8	−8.1	−6	−7	19.4	21	20.2
BT5-55	Vein-cal	3	108.2	113.8	111.7	−4.8	−3.5	−4.3	17.3	18.5	18.1
BT5-21	Vein-cal	4	138.3	146.7	141.7	−0.3	−8.7	−9.1	21.5	22.6	21.8

**Figure 10.** (A) T_h of fluid inclusions in D2 and D3 dolomites, and vein calcite. (B) Cross-plot of T_h versus salinity. The salinity was calculated from T_m of fluid inclusions in D2 and D3 dolomites, and vein calcite.

5. Discussion

5.1. Genesis of D1 Dolomite

D1 dolomite consists of extremely fine crystals (20–60 μm) with nonplanar fabric, which may be associated with the penecontemporaneous dolomitization at the relatively low temperature of near-surface conditions [6,7,49]. It is generally believed that the critical roughening temperature (CRT) of nonplanar dolomite crystals is 50–60 $^{\circ}\text{C}$ [42]. When the ambient temperature is below this temperature, the formation of dolomite requires a supersaturated fluid with extremely high Mg-ion concentrations with respect to dolomite [7,36,50]. Moreover, bacterial sulfate reduction (BSR) has been reported to promote dolomite precipitation under the near-surface, low-temperature conditions by reducing the kinetic barrier [18,51,52]. BSR tends to occur in a reducing environment with the extensive presence of Fe^{2+} , which is prone to forming pyrite [53]. The amorphous to cryptocrystalline pyrites are widely distributed in the intercrystalline pores, suggesting that the formation of D1 dolomite is potentially related to the BSR (Figure 3C).

The $\delta^{13}\text{C}$ values of D1 dolomite mostly overlap with the ranges of the $\delta^{13}\text{C}$ values for the ambient limestones (−1.30 to −0.30‰ VPDB) and the reported calcites in equilibrium with Cambrian seawater (−2.5 to +1.0‰ VPDB) [45,46]. Numerous studies have shown that, except for diagenetic systems with enormous water/rock ratios, the effect of diagenesis on the carbonate isotopic composition in carbonate rocks is relatively limited [54]. Therefore, D1 dolomite may be formed in the penecontemporaneous dolomitization caused by the progressive refluxing seawater or the evaporative seawater in the tidal flat, and retains the carbon isotopic feature of original seawater. Restricted environments and evaporative conditions have kinetic conditions that favor dolomite formation [36]. The lower $\delta^{13}\text{C}$ values of D1 dolomite than the estimated $\delta^{13}\text{C}$ range of coeval calcite may be related to BSR. It is well known that the $\delta^{13}\text{C}$ of the primeval BSR dolomites is generally less than −20‰

VPDB [55]. The D1 dolomite may have originated from the dolomite nuclei formed by BSR in the early stage, being further dolomitized by the refluxing seawater in the late stage.

The $\delta^{18}\text{O}$ values of D1 dolomite (-7.22 to -4.70‰ VPDB) all fall within the ranges of $\delta^{18}\text{O}$ for the estimated Cambrian marine dolomites (-8.0 to -3.0‰ VPDB) [18]. The study area was located in the platform interior during the Cambrian. The warm, semiarid to arid climate and restriction in seawater circulation contribute to intense evaporation, which increases seawater salinity. The evaporative deposits, such as gypsum, are widespread throughout the logged core intervals in the Middle Cambrian. Dolomites precipitated in the evaporated seawater environment tend to possess high-oxygen isotopes [48].

Moreover, the $^{87}\text{Sr}/^{86}\text{Sr}$ values of D1 dolomite (0.709039 to 0.709158) are similar to the $^{87}\text{Sr}/^{86}\text{Sr}$ values of the ambient limestones (0.708872 to 0.709354), and are in line with the estimated $^{87}\text{Sr}/^{86}\text{Sr}$ ranges (0.7085–0.7095) of the coeval seawater [45,46]. This suggests that the dolomitizing fluid of D1 dolomite was primarily attributed to the coeval evaporated seawater. In tidal flat and lagoon environments, intense evaporation leads to the concentration of Mg ions, forming Mg-rich brines, which dolomitize the near-surface carbonate deposits [11,12,15]. However, the $\delta^{18}\text{O}$ values of D1 dolomite are lower than those of estimated evaporative dolomites (-3.5 to 2.0‰ VPDB) [48], indicating that D1 dolomite is formed in the mesosaline to penesaline seawaters, rather than the evaporated hypersaline brines [18].

The PAAS-normalized REE patterns of D1 dolomite are consistent with those of the surrounding limestones, which suggest that the dolomitizing fluid of D1 dolomite originates from original seawater (Figure 7A,D). In addition, the high Na, Sr and Fe abundances, as well as the low Mn abundance of D1 dolomite, also prove that D1 dolomite was formed in the penecontemporaneous stage.

In addition, the Mn and Sr abundance of D1 dolomite shows a negative correlation (Figure 6B). Typically, recrystallization and burial diagenesis would reduce Sr abundance and increase Mn abundance in dolomite [48]. This indicates that D1 dolomite may experience replacement or recrystallization. The cation ordering values of D1 dolomite (average 0.83) are slightly higher than those of common sedimentary dolomite (0.54~0.66) [36], which also indicates that it may have undergone recrystallization or burial diagenesis. However, recrystallization or burial diagenesis has a weak influence on D1 dolomite due to the high Sr abundances (2890 ppm) and low Mn/Sr ratios (<2.0) of D1 dolomite.

5.2. Genesis of D2 Dolomite

Compared with D1 dolomite, D2 dolomite has a larger crystal size distribution and is dominated by nonplanar and planar-s crystals. D2 dolomite displays well-preserved primary sedimentary structures of precursor limestone, such as ooid and grained clast (Figure 4A,C,D), which are characteristic features common in shallow shoal environments. Meanwhile, the $\delta^{13}\text{C}$ values of D2 dolomite are highly coincident with the $\delta^{13}\text{C}$ values of surrounding limestones, and within the $\delta^{13}\text{C}$ range reported for the coeval marine calcites, indicating that the $\delta^{13}\text{C}$ feature of D2 dolomite originates from the connate seawater. This is in line with the characteristics of the seepage–reflux dolomitization model, where the progressive refluxing seawater from tidal flats or lagoons derived from fluid density fluctuation or eustatic sea level changes seeps back into the porous precursor limestone, leading to pervasive dolomitization due to dolomite replacement, precipitation, and overgrowth [6,52].

In addition, D2 dolomite is present as subhedral to euhedral crystal clusters or floating dolomite rhombohedrons along the stylolites (Figure 4A). This suggests that the formation of D2 dolomite may be related to the compaction and dissolution during the shallow burial setting. Previous studies have shown that stylolites in carbonate rocks mostly start at a burial depth of approximately 500 m [18,56]. As the carbonates are buried to a certain depth (usually 500–1000 m or deeper), Mg-rich rocks (argillaceous limestones or siliciclastic rocks) will release Mg ions under compaction and solution, thereby increasing the Mg concentration of the connate seawater preserved in the host limestones/dolomites. The

chemically modified seawater migrates along the stylolites and replaces or recrystallizes the precursor limestone/dolomite [57] or causes the nucleation of dolomite crystals and their subsequent overgrowth [14]. Insufficient dolomitizing fluid in the nucleation zone may lead to partial dolomitization, resulting in floating D2 dolomite crystals (Figure 4B).

The $^{87}\text{Sr}/^{86}\text{Sr}$ ratios of D2 dolomite are significantly higher than the estimated $^{87}\text{Sr}/^{86}\text{Sr}$ ratios of Cambrian seawater (Figure 9), indicating that its dolomitizing fluid is richer in the ^{87}Sr than the original seawater. It is reported that the Precambrian basement in the study area is composed of enormous felsic siliciclastic rocks and magmatic rocks rich in $^{87}\text{Sr}/^{86}\text{Sr}$ ratios [58]. The ^{87}Sr -rich deep hydrothermal fluids may have migrated from the Precambrian basement to the Cambrian carbonate rocks through fractures, causing replacement or recrystallization.

This interpretation is also supported by the $\delta^{18}\text{O}$ and fluid inclusion evidence. The temperature of dolomitizing fluid represented by the Th of D2 dolomite (73.3–108.1 °C) exceeds the estimated burial temperature, indicating a hydrothermal fluid. Depending on the calcite–fluid fractionation equation proposed by Land (1983) [5], considering the $\delta^{18}\text{O}$ value of the ambient limestones (−9.9 to −7.3‰ VPDB) in Cambrian successions, and taking into account an average surface temperature of 20 °C, the $\delta^{18}\text{O}$ values of the Cambrian seawater ranged from −9.65 to −6.97‰ VSMOW. Considering a surface temperature of 20 °C and an average geothermal gradient in the Cambrian of 30–35 °C/km [32], based on the dolomite–fluid fractionation equation of Land (1983) [5], combined with the $\delta^{18}\text{O}$ values of D2 dolomite, it is concluded that the $\delta^{18}\text{O}$ value of dolomitizing fluid that forms D2 dolomite should be 1.1 to 4.6‰ VSMOW (Figure 11). The $\delta^{18}\text{O}$ values of dolomitizing fluid are significantly larger than the estimated $\delta^{18}\text{O}$ values of Cambrian seawater, but similar to the reported $\delta^{18}\text{O}$ values of hydrothermal fluid and residual brine [59]. In addition, the positive Eu anomaly of D2 dolomite also suggests that the formation of D2 dolomite is closely related to deep hydrothermal fluid. The acidic hydrothermal fluid entering the host carbonate rocks is prone to modifying the REE composition of dolomite through diagenesis [60,61].

The low Sr abundance (175 ppm) and high cation ordering (average 0.93) of D2 dolomite indicate that in the deep burial stage, D2 dolomite experienced recrystallization or buried diagenesis, and the superposition of multiple diagenesis complicates the dolomite geochemical properties.

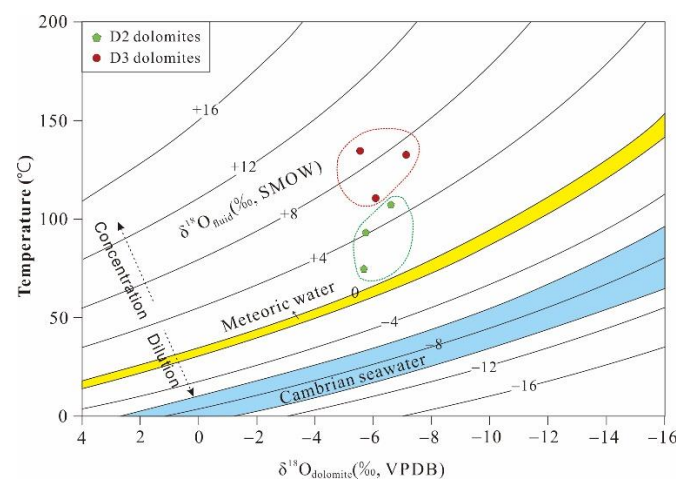


Figure 11. Cross-plot of $\delta^{18}\text{O}$ values (VPDB) versus homogenization temperatures of D2 and D3 dolomites. Curved lines are isopleths for $\delta^{18}\text{O}_{\text{fluid}}$ calculated using the dolomite–fluid oxygen isotope fractionation equations [5].

5.3. Genesis of D3 Dolomite

D3 dolomite is characterized by medium to coarse crystals with planar-s and planar-e textures (Figure 5). The dolomite crystal with a cloudy core and compositional zoning

commonly indicates that different dolomitizing fluids participated in diagenesis at different stages. (Figure 5A–E) [4,6,23]. The cloudy core may be caused by the high-salinity fluids in the shallow burial condition, while the bright rim may be formed from the low-salinity fluid in the deep burial condition. The compositional zoning of dolomite crystal usually arises from the intense recrystallization of previously formed dolomite in a deep burial setting. The saddle-shaped crystals and tightly packed anhedral texture of D3 dolomite (Figure 5D,E) suggest the rapid growth of disordered crystals at elevated temperatures [17,31,42]. The high cation ordering (average 0.91), low Sr abundance (average 176 ppm) and high Mn/Sr ratio also suggest that D3 dolomite has undergone strong recrystallization. The recrystallization and the compaction and dissolution during the deep burial stage ultimately destroy the original sedimentary fabric of the precursor dolomite [6].

The large overlap of $\delta^{13}\text{C}$ values among the D1, D2, and D3 dolomites and surrounding limestones (Figure 8), as well as the similar PAAS-normalized REE pattern (Figure 7), indicates that D3 dolomite is likely the result of the dolomitization and recrystallization of the precursor dolomite or limestone. The $\delta^{18}\text{O}$ values of D3 dolomite are significantly lower than those of D1 and D2 dolomites, indicating that D3 dolomite was formed at a higher temperature. The Th of D3 dolomite ranges from 104.6 to 140.8 °C, suggesting that the burial depth of dolomitization may be 2500–4000 m. According to the dolomite–fluid fractionation equation of Land (1983) [5], combined with the $\delta^{18}\text{O}$ values of D3 dolomite, the $\delta^{18}\text{O}$ value of the dolomitizing fluid that forms D3 dolomite should be 5.5 to 8.6‰ VSMOW (Figure 11). The $\delta^{18}\text{O}$ values of dolomitizing fluid that forms D3 dolomite are significantly higher than the $\delta^{18}\text{O}$ values of the Cambrian seawater and the dolomitizing fluid that forms D2 dolomite. The continuous fluid–rock interaction through faults/fractures with ^{18}O -rich minerals may enhance the temperature and oxygen isotopes of the dolomitizing fluid. For example, anhydrite, which is widely distributed in the study area, has a $\delta^{18}\text{O}$ value of up to 20.8‰ VPDB [62]. The $^{87}\text{Sr}/^{86}\text{Sr}$ ratios of D3 dolomite were significantly higher than those of D1 and D2 dolomites, and the surrounding limestone (Figure 11), indicating that the fluids with higher radioactive Sr participated in the dolomitization process. During the deep burial condition, the fluid–rock interaction is enhanced due to the high temperature and pressure, resulting in an increase in ^{87}Sr -rich fluids in deep sedimentary formations [49].

5.4. Timing of Dolomitization Episodes

The studies on the origin of dolomite show that the Cambrian dolomites in the study area have experienced multiple stages of dolomitization.

D1 dolomite was mainly formed in the near-surface penecontemporaneous stage with a burial depth of less than 500 m and an ambient temperature of less than 50 °C. The intense evaporation and restricted seawater environment in the study area prompted the Mg/Ca ratio of seawater, resulting in the mesosaline to penesaline dolomitizing fluid. The BSR during the deposition of the Cambrian carbonates contributed to the formation of dolomite seed crystals. The micrite calcite formed in the primitive seawater diagenetic environment was dolomitized during the seepage of evaporatively concentrated seawater, forming massive dolomite and growing continuously.

D2 dolomite was primarily formed by the seepage–reflux dolomitization during the shallow burial stage. The evaporated seawater in tidal flats and lagoons infiltrates downwards, driven by the fluid density fluctuation or eustatic sea level change, and dolomitizes the underlying porous shoal limestone [19,28]. Meanwhile, the formation of D2 dolomite is also related to the hydrothermal activity and pressure dissolution. The tectonic movements in the Cambrian, such as the Pan-African orogeny of approximately 550 Ma, formed numerous fractures, connecting the upper formation with the Precambrian basement. The connate seawater preserved in formation infiltrates into the basement along the fractures; absorbs the active elements of Mg, Fe, Mn, and Sr in the surrounding rock under the action of the water–rock interactions; mixes with hydrothermal fluid and deep-basinal brine; and then returns to the upper strata. The mixed fluid migrates along the

stylolite and fracture formed by the pressure dissolution in the Cambrian carbonate rocks and dolomitizes the precursor limestone around the channel.

D3 dolomite was chiefly formed in the deep burial stage with a burial depth from 2500 m to 4000 m and an ambient temperature of less than 150 °C. As shown in Figure 2, the Cambrian in the study area subsided continuously and rapidly after deposition. During the Middle to Late Ordovician, the burial depth of Cambrian carbonate rocks was approximately 4000–5000 m, and the temperature was approximately 140–180 °C. The sustained high-temperature and high-pressure conditions during the deep burial stage enhanced the recrystallization and burial dolomitization. The connate seawater, hydrothermal fluid and deep-basinal brine in the formation circulate in fractures driven by geothermal variation, and undergo a fluid–rock reaction with the surrounding rock, providing Mg ions for dolomitization and recrystallization in the deep burial stage. Eventually, the dolomitization ceases due to the insufficient supply of Mg ions in the formation fluid, and the calcite and quartz cements precipitate and fill the intercrystalline pores of the dolomite, such as the calcite vein with high T_h in D2 and D3 dolomites (Figure 10).

Generally, the Cambrian dolomitizing fluid in the study area was dominated by, or essentially derived from, the seawater, and the depth of seawater dolomitization was widely distributed. The penecontemporaneous very fine-crystalline dolomite and shallow-burial fine-crystalline dolomite formed in the original marine environment dominates the Cambrian dolomite rocks in the study area and contributes to pervasive dolomitization in the form of seeds. Due to long-term deep burial, the Cambrian dolomite has experienced varying degrees of recrystallization and burial diagenesis. Especially near the areas with abundant fractures, the deep circular fluid completely modifies the original structure of the precursor limestone or dolomite through recrystallization and burial diagenesis and forms considerable medium- and coarse-crystalline dolomite.

6. Conclusions

- (1) Three types of matrix dolomites were identified from the Cambrian dolomite in the study area: very fine-crystalline, nonplanar dolomite (D1); fine-crystalline, nonplanar to planar-s dolomite (D2); and medium- to coarse-crystalline, planar-e to planar-s dolomite (D3).
- (2) D1 dolomite is a primarily penecontemporaneous dolomite formed in coeval evaporated seawater, and is weakly affected by deep burial diagenesis.
- (3) D2 dolomite is the chief product of seepage–reflux dolomitization during the shallow burial stage, and is closely related to hydrothermal fluid and pressure dissolution.
- (4) D3 dolomite is principally formed by the recrystallization of precursor carbonate rocks in the deep burial stage under relatively high temperature and pressure conditions.

Author Contributions: Conceptualization, Z.C. and Y.Y.; methodology, Z.C. and P.W.; investigation, Z.C., S.Z. and W.D.; resources, C.D. and N.L.; writing—original draft preparation, Z.C. and Y.Y.; writing—review and editing, Z.C., S.Z. and W.D.; visualization, Y.Y. and Y.L.; supervision, S.Z. and W.D.; funding acquisition, C.D. and N.L. All authors have read and agreed to the published version of the manuscript.

Funding: This research was supported by National Natural Science Foundation of China (42102177), Natural Science Foundation of Shanxi Province of China (2021JQ-592), and Shaanxi Provincial Educational Department (21JK0840).

Acknowledgments: We thank Qicong Wang (Xi'an Shiyou University), Bo Zhou (SINOPEC), and Lianqi Jia (Northwest University) for their assistance in petrographic and geochemical analysis. We also thank the associate editor and the reviewers for their helpful recommendations and constructive suggestions.

Conflicts of Interest: The authors declare no conflict of interest.

References

1. Zhao, W.Z.; Shen, A.J.; Hu, A.P.; Zhou, J.G.; Ni, X.F. A discussion on the geological background of marine carbonate reservoirs development in Tarim, Sichuan and Ordos Basin, China. *Acta Petrol. Sin.* **2015**, *31*, 3495–3508.
2. Ding, W.L.; Qi, L.X.; Yun, L.; Yu, T.X.; Wu, L.M.; Cao, Z.C.; You, S.G. The tectonic evolution and its controlling effects on the development of Ordovician reservoir in Bachu-Markit Tarim basin. *Acta Petrol. Sin.* **2012**, *28*, 2542–2556.
3. Han, C.; Lin, C.; Lu, X.; Tian, J.; Ren, L.; Ma, C. Petrological and geochemical constraints on fluid types and formation mechanisms of the ordovician carbonate reservoirs in Tahe oilfield, Tarim basin, NW China. *J. Pet. Sci. Eng.* **2019**, *178*, 106–120. [[CrossRef](#)]
4. Ye, N.; Zhang, S.; Qing, H.; Li, Y.; Liu, D. Dolomitization and its impact on porosity development and preservation in the deeply burial Lower Ordovician carbonate rocks of Tarim Basin, NW China. *J. Pet. Sci. Eng.* **2019**, *182*, 106303. [[CrossRef](#)]
5. Land, L.S. The application of stable isotopes to studies of the origin of dolomite and to problems of diagenesis of clastic sediments. In *Stable Isotopes in the Sedimentary Geology*; SEPM Short Course Notes; Arthur, M.A., Anderson, T.F., Kaplan, I.R., Veizer, J., Land, L.S., Eds.; Geo Science World: McLean, VA, USA, 1983; Volume 10, pp. 4.1–4.22.
6. Machel, H.G. Concepts and models of dolomitization: A critical reappraisal. In *The Geometry and Petrogenesis of Dolomite Hydrocarbon Reservoirs*; Special Publication; Braithwaite, C.J.R., Rizzi, G., Darke, G., Eds.; The Geological Society of London: London, UK, 2004; Volume 235, pp. 7–63.
7. Warren, J. Dolomite: Occurrence, evolution and economically important associations. *Earth-Sci. Rev.* **2000**, *52*, 1–81. [[CrossRef](#)]
8. Jones, G.D.; Xiao, Y. Dolomitization, anhydrite cementation, and porosity evolution in a reflux system: Insights from reactive transport models. *AAPG Bull.* **2005**, *89*, 577–601. [[CrossRef](#)]
9. Zhao, W.Z.; Shen, A.J.; Qiao, Z.F.; Pan, L.Y.; Hu, A.P.; Zhang, J. Genetic types and distinguished characteristics of dolomite and the origin of dolomite reservoirs. *Petrol. Explor. Dev.* **2018**, *45*, 983–997. [[CrossRef](#)]
10. Azomani, E.; Azmy, K.; Blamey, N.; Brand, U.; Al-Aasm, I. Origin of Lower Ordovician dolomites in eastern Laurentia: Controls on porosity and implications from geochemistry. *Mar. Petrol. Geol.* **2013**, *40*, 99–114. [[CrossRef](#)]
11. Kaufman, A.J.; Jacobsen, S.B.; Knoll, A.H. The Vendian record of Sr and C isotopic variations in seawater: Implications for tectonics and paleoclimate. *Earth Planet. Sci. Lett.* **1993**, *120*, 409–430. [[CrossRef](#)]
12. Jones, G.D.; Whitaker, F.F.; Smart, P.L.; Sanford, W.E. Numerical analysis of seawater circulation in carbonate platforms: II. The dynamic interaction between geothermal and brine reflux circulation. *Am. J. Sci.* **2004**, *304*, 250–284. [[CrossRef](#)]
13. Qing, H.R.; Veizer, J. Oxygen and carbon isotopic composition of Ordovician brachiopods: Implications for coeval seawater. *Geochim. Cosmochim. Acta* **1994**, *58*, 4429–4442. [[CrossRef](#)]
14. Machel, H.G.; Buschkuehle, B.E. Diagenesis of the Devonian Southesk-Cairn Carbonate complex, Alberta, Canada: Marine cementation, burial dolomitization, thermochemical sulfate reduction, anhydritization, and squeegee fluid flow. *J. Sediment. Res.* **2008**, *78*, 366–389. [[CrossRef](#)]
15. Shao, L.; He, H.; Peng, S.; Li, R.J. Types and origin of dolostones of the Cambrian and Ordovician of Bachu Uplift area in Tarim Basin. *J. Palaeogeogr.* **2002**, *4*, 19–30.
16. Lavoie, D.; Ghi, G.; Brennan-Alpert, P.; Desrochers, A.; Bertrand, R. Hydrothermal dolomitization in the lower Ordovician romaine formation of the Anticosti basin: Significance for hydrocarbon exploration. *Bull. Can. Petrol. Geol.* **2005**, *53*, 454–471. [[CrossRef](#)]
17. Davies, G.R.; Smith, L.B. Structurally controlled hydrothermal dolomite reservoir facies: An overview. *AAPG Bull.* **2006**, *90*, 1641–1690. [[CrossRef](#)]
18. Guo, C.; Chen, D.; Qing, H.; Dong, S.; Li, G.; Wang, D.; Qian, Y.; Liu, C. Multiple dolomitization and later hydrothermal alteration on the upper cambrian-lower ordovician carbonates in the northern tarim basin, china. *Mar. Pet. Geol.* **2016**, *72*, 295–316. [[CrossRef](#)]
19. Wang, X.L.; Jin, Z.J.; Hu, W.X.; Zhang, J.T.; Qian, Y.X.; Zhu, J.Q.; Li, Q. Using in situ REE analysis to study the origin and diagenesis of dolomite of Lower Palaeozoic, Tarim Basin. *Sci. China Ser. D Earth Sci.* **2009**, *52*, 681–693, (In Chinese with English Abstract). [[CrossRef](#)]
20. Vasconcelos, C.; McKenzie, J.A. Microbial mediation of modern dolomite precipitation and diagenesis under anoxic conditions (Lagoa Vermelha, Rio de Janeiro, Brazil). *J. Sediment. Res.* **1997**, *67*, 378–390.
21. Zheng, J.; Zhu, Y.; Huang, L.; Yang, G.; Hu, F. Geochemical Characteristics and Their Geological Significance of Lower Cambrian Xiaerblak Formation in Northwestern Tarim Basin, China. *Minerals* **2022**, *12*, 781. [[CrossRef](#)]
22. Hu, M.Y.; Ngia, N.R.; Gao, D. Dolomitization and hydrotectonic model of burial dolomitization of the Furongian-Lower Ordovician carbonates in the Tazhong Uplift, central Tarim Basin, NW China: Implications from petrography and geochemistry. *Mar. Pet. Geol.* **2019**, *106*, 88–115. [[CrossRef](#)]
23. Jiang, L.; Cai, C.F.; Worden, R.H.; Crowley, S.F.; Jia, L.; Zhang, K.; Duncan, I.J. Multiphase dolomitization of deeply buried Cambrian petroleum reservoirs, Tarim Basin, north-west China. *Sedimentology* **2016**, *63*, 2130–2157. [[CrossRef](#)]
24. Al-Aasm, I.; Ionnee, J.; Clarke, J. Multiple fluid flow events and the formation of saddle dolomite: Examples from middle Devonian carbonates of the western Canadian Basin. *J. Geochem. Explor.* **2000**, *69–70*, 11–15. [[CrossRef](#)]
25. Wei, M.; Bao, Z.; Munnecke, A.; Liu, W.; Harrison, G.W.M.; Zhang, H.; Zhang, D.; Li, Z.; Xu, X.; Lu, K.; et al. Paleoenvironment of the Lower–Middle Cambrian Evaporite Series in the Tarim Basin and Its Impact on the Organic Matter Enrichment of Shallow Water Source Rocks. *Minerals* **2021**, *11*, 659. [[CrossRef](#)]

26. Wu, G.H.; Li, H.W.; Xu, Y.L.; Su, W.; Chen, Z.Y.; Zhang, B.S. The tectonothermal events, architecture and evolution of Tarim craton basement palaeo-uplifts. *Acta Petrol. Sin.* **2012**, *28*, 2435–2452.
27. Lin, C.T.; Li, S.T.; Liu, J.Y.; Qian, Y.X.; Luo, H.; Chen, J.Q.; Peng, L.X.; Rui, Z.F. Tectonic framework and paleogeographic evolution of the Tarim basin during the Paleozoic major evolutionary stages. *Acta Petrol. Sin.* **2010**, *27*, 210–218.
28. Du, Y.; Fan, T.; Machel, H.G.; Gao, Z. Genesis of Upper Cambrian-lower ordovician dolomites in the Tahe oilfield, Tarim Basin, NW China: Several limitations from petrology, geochemistry, and fluid inclusions. *Mar. Pet. Geol.* **2017**, *91*, 43–70. [[CrossRef](#)]
29. Gao, Z.Q.; Fan, T.L. Carbonate platform-margin architecture and its influence on Cambrian-Ordovician reef-shoal development, Tarim Basin, NW China. *Mar. Petrol. Geol.* **2015**, *68*, 291–306. [[CrossRef](#)]
30. Lin, C.S.; Yang, H.J.; Liu, J.Y.; Peng, L.; Cai, Z.Z.; Yang, X.F.; Yang, Y.H. Paleostuctural geomorphology of the Paleozoic central uplift belt and its constraint on the development of depositional facies in the Tarim Basin. *Sci. Chin. Ser. D Earth Sci.* **2009**, *52*, 823–834. [[CrossRef](#)]
31. Ngia, N.R.; Hu, M.Y.; Gao, D. Tectonic and geothermal controls on dolomitization and dolomitizing fluid flows in the Cambrian-Lower Ordovician carbonate successions in the western and central Tarim Basin, NW China. *J. Asian Earth Sci.* **2019**, *172*, 359–382. [[CrossRef](#)]
32. Qiu, N.S.; Chang, J.; Zuo, Y.H.; Wang, J.Y.; Li, H.L. Thermal evolution and maturation of lower Paleozoic source rocks in the Tarim Basin, Northwest China. *AAPG Bull.* **2012**, *96*, 789–821. [[CrossRef](#)]
33. Goldsmith, J.R.; Graf, D.L. Structural and compositional variations in some natural dolomites. *J. Geol.* **1958**, *66*, 678–693. [[CrossRef](#)]
34. Fang, Y.; Xu, H. A new approach to quantify the ordering state of protodolomite using XRD, TEM, and Z-contrast imaging. *J. Sediment. Res.* **2019**, *89*, 537–551. [[CrossRef](#)]
35. Stephen, E.K.; Duncan, F.S. On the evolution of dolomite stoichiometry and cation order during high-temperature synthesis experiments: An alternative model for the geochemical evolution of natural dolomites. *Sediment. Geol.* **2011**, *240*, 30–40.
36. Manche, C.J.; Kaczmarek, S.E. A global study of dolomite stoichiometry and cation ordering through the phanerozoic. *J. Sediment. Res.* **2021**, *91*, 520–546. [[CrossRef](#)]
37. McLennan, S. Rare earth elements in sedimentary rocks: Influence of provenance and sedimentary processes. *Rev. Mineral. Geochem* **1989**, *21*, 169–200.
38. Bau, M.; Dulski, P. Controls on the fractionation of isovalent trace elements in magmatic and aqueous systems: Evidence from Y/Ho, Zr/Hf, and lanthanide tetrad effect. *Contrib. Mineral. Petrol.* **1996**, *123*, 323–333. [[CrossRef](#)]
39. Kim, S.T.; Coplen, T.B.; Horita, J. Normalization of stable isotope data for carbonate minerals: Implementation of iupac guidelines. *Geochim. Cosmochim. Acta* **2015**, *158*, 276–289. [[CrossRef](#)]
40. Zhang, W.; Hu, Z.; Liu, Y. Iso-Compass: New freeware software for isotopic data reduction of LA-MC-ICP-MS. *J. Anal. At. Spectrom.* **2020**, *35*, 1087–1096. [[CrossRef](#)]
41. Bodnar, R. Revised equation and table for determining the freezing point depression of H₂O-NaCl solutions. *Geochim. Cosmochim. Acta* **1993**, *57*, 683–684. [[CrossRef](#)]
42. Sibley, D.F.; Gregg, J.M. Classification of dolomite rock textures. *J. Sediment. Petrol.* **1987**, *57*, 967–975.
43. Derry, L.A.; Brasier, M.D.; Corfield, R.M.; Rozanov, A.Y.; Zhuravlev, A.Y. Sr and C isotopes in Lower Cambrian carbonates from the Siberian craton: A paleoenvironmental record during the ‘Cambrian explosion’. *Earth Planet. Sci. Lett.* **1994**, *128*, 678–681. [[CrossRef](#)]
44. Sun, S.S.; McDonough, W.F. Chemical and Isotopic Systematics of Oceanic Basalts: Implications for Mantle Composition and Processes. *Geol. Soc. Lond. Spec. Publ.* **1989**, *42*, 313–345. [[CrossRef](#)]
45. Veizer, J.; Ala, D.; Azmy, K.; Bruckschen, P.; Buhl, D.; Bruhn, F.; Carden, G.A.F.; Diener, A.; Ebner, S.; Godderis, Y.; et al. ⁸⁷Sr/⁸⁶Sr, ^δ¹³C and ^δ¹⁸O evolution of Phanerozoic seawater. *Chem. Geol.* **1999**, *161*, 59–88. [[CrossRef](#)]
46. Montañez, I.P.; Osleger, D.A.; Mack, L.E.; Banner, J.L.; Mack, L.E.; Musgrove, M.L. Evolution of the Sr and C isotope composition of Cambrian Oceans. *GSA Today* **2000**, *10*, 1–7.
47. Land, L.S. The isotopic and trace element geochemistry of dolomite: The state of the art. In *Concepts and Models of Dolomitization*; SEPM Special Publication; Zenger, D.H., Dunham, J.B., Ethington, R.L., Eds.; Geo Science World: McLean, VA, USA, 1980; Volume 28, pp. 87–110.
48. Montañez, I.P.; Read, J.F. Fluid-rock interaction history during stabilization of early dolomites, upper Knox Group (Lower Ordovician), US Appalachians. *J. Sediment. Petrol.* **1992**, *62*, 753–778.
49. Al-Aasm, I.S.; Packard, J.J. Stabilization of early-formed dolomite: A tale of divergence from two Mississippian dolomites. *Sediment. Geol.* **2000**, *131*, 97–108. [[CrossRef](#)]
50. Meister, P.; McKenzie, J.A.; Bernasconi, S.M.; Brack, P. Dolomite formation in the shallow seas of the Alpine Triassic. *Sedimentology* **2013**, *60*, 270–291. [[CrossRef](#)]
51. Baldermann, A.; Deditius, A.P.; Dietzel, M.; Fichtner, V.; Fischer, C.; Hippler, D.; Leis, A.; Baldermann, C.; Mavromatis, V.; Stickler, C.P. The role of bacterial sulfate reduction during dolomite precipitation: Implications from Upper Jurassic platform carbonates. *Chem. Geol.* **2015**, *412*, 1–14. [[CrossRef](#)]
52. Preto, N.; Breda, A.; Dal Corso, J.; Spotl, C.; Zorzi, F.; Frisia, S. Primary dolomite in the late Triassic Travenanzes formation, dolomites, northern Italy: Facies control and possible bacterial influence. *Sedimentology* **2015**, *62*, 697–716. [[CrossRef](#)]
53. Vuillemin, A.; Ndiaye, M.; Martini, R.; Davaud, E. Cement stratigraphy: Image probes of cathodoluminescent facies. *Swiss J. Geosci.* **2011**, *104*, 55–66. [[CrossRef](#)]

54. Kump, L.R. Interpreting carbon-isotope excursions: Strangelove oceans. *Geology* **1991**, *19*, 299–302. [[CrossRef](#)]
55. Van Lith, Y.; Warthmann, R.; Vasconcelos, C.; McKenzie, J.A. Sulphatereducing bacteria induce low-temperature Ca-dolomite and high Mg-calcite formation. *Geobiology* **2003**, *1*, 71–79. [[CrossRef](#)]
56. Fabricius, I.L.; Borre, M.K. Stylolites, porosity, depositional textures, and silicates in chalk facies sediments. Ontong Java Plateau-Gorm and Tyra fields, North Sea. *Sedimentology* **2007**, *54*, 183–205. [[CrossRef](#)]
57. Choquette, P.W.; Hiatt, E.E. Shallow-burial dolomite cement: A major component of many ancient sucrosic dolomites. *Sedimentology* **2008**, *55*, 423–460. [[CrossRef](#)]
58. Zhai, M. The main old lands in China and assembly of Chinese unified continent. *Sci. China (Ser. D Geol.)* **2013**, *56*, 1829–1852. [[CrossRef](#)]
59. Goldstein, R.H.; Reynolds, T.J. *Systematics of Fluid Inclusions in Diagenetic Minerals*; Society for Sedimentary Geology (SEPM) Short Course; SEPM: Tulsa, OK, USA, 1994.
60. Ryan, B.; Kaczmarek, S.; Rivers, J.; Manche, C. Extensive recrystallization of Cenozoic dolomite during shallow burial: A case study from the Palaeocene–Eocene Umm er Radhuma Formation and a global meta-analysis. *Sedimentology* **2022**, *69*, 2053–2079. [[CrossRef](#)]
61. Kučera, J.; Cempirek, J.; Dolnicek, Z.; Muchez, P.; Prochaska, W. Rare earth elements and yttrium geochemistry of dolomite from post-Variscan vein-type mineralization of the Nizky Jeseník and Upper Silesian Basins, Czech Republic. *J. Geochem. Explor.* **2009**, *103*, 69–79. [[CrossRef](#)]
62. Jiang, L.; Worden, R.H.; Cai, C.F. Generation of isotopically and compositionally distinct water during thermochemical sulfate reduction (TSR) in carbonate reservoirs: Triassic Feixianguan Formation, Sichuan Basin, China. *Geochim. Cosmochim. Acta* **2015**, *165*, 249–262. [[CrossRef](#)]